

Microscale Heat Transfer

ANDREW N. SMITH

Department of Mechanical Engineering
United States Naval Academy
Annapolis, Maryland

PAMELA M. NORRIS

Department of Mechanical and Aerospace Engineering
University of Virginia
Charlottesville, Virginia

- 18.1 Introduction
- 18.2 Microscopic description of solids
 - 18.2.1 Crystalline structure
 - 18.2.2 Energy carriers
 - 18.2.3 Free electron gas
 - 18.2.4 Vibrational modes of a crystal
 - 18.2.5 Heat capacity
 - Electron heat capacity
 - Phonon heat capacity
 - 18.2.6 Thermal conductivity
 - Electron thermal conductivity in metals
 - Lattice thermal conductivity
- 18.3 Modeling
 - 18.3.1 Continuum models
 - 18.3.2 Boltzmann transport equation
 - Phonons
 - Electrons
 - 18.3.3 Molecular approach
- 18.4 Observation
 - 18.4.1 Scanning thermal microscopy
 - 18.4.2 3ω technique
 - 18.4.3 Transient thermorefectance technique
- 18.5 Applications
 - 18.5.1 Microelectronics applications
 - 18.5.2 Multilayer thin-film structures
- 18.6 Conclusions
- Nomenclature
- References

18.1 INTRODUCTION

The microelectronics industry has been driving home the idea of miniaturization for the past several decades. Smaller devices equate to faster operational speeds and more transportable and compact systems. This trend toward miniaturization has an infectious quality, and advances in nanotechnology and thin-film processing have spread to a wide range of technological areas. A few examples of areas that have been affected significantly by these technological advances include diode lasers, photovoltaic cells, thermoelectric materials, and microelectromechanical systems (MEMS). Improvements in the design of these devices have come mainly through experimentation and macroscale measurements of quantities such as overall device performance. Most studies of the microscale properties of these devices and materials have focused on either electrical and/or microstructural properties. Numerous thermal issues, which have been largely overlooked, currently limit the performance of modern devices. Hence the thermal properties of these materials and devices are of critical importance for the continued development of high-tech systems.

The need for increased understanding of the energy transport mechanisms of thin films has given rise to a new field of study called *microscale heat transfer*. Microscale heat transfer is simply the study of thermal energy transfer when the individual carriers must be considered or when the continuum model breaks down. The continuum model for heat transfer has classically been the conservation of energy coupled with Fourier's law for thermal conduction. In an analogous manner, the study of "gas dynamics" arose when the continuum fluid mechanics models were insufficient to explain certain phenomena. The field of microscale heat transfer bears some striking similarities. One area of similarity is in the methodology. Usually, the first attempt at modeling is to modify the continuum model in such a way that the microscale considerations are taken into account. The more common and slightly more difficult method is application of the Boltzmann transport equation. Finally, when both of these methods fail, the computationally exhaustive molecular dynamics approach is typically adopted. These three methods and specific applications will be discussed in more detail.

Figure 18.1 demonstrates four different mechanisms by which electrons, the primary heat carriers in metallic films, can be scattered. All of these scattering mechanisms are important in the study of microscale heat transfer. The mean free path of an electron in a bulk metal is typically on the order of 10 to 30 nm, where electron lattice scattering is dominant. However, when the film thickness is on the order of the mean free path, boundary scattering comes important. This is referred to as a *size effect* because the physical size of the film influences the transport properties. Thin films are manufactured using a number of methods and under a wide variety of conditions. This can have a serious influence on the microstructure of the film, which influences defect and grain boundary scattering. Finally, when heated by ultrashort pulses, the electron system becomes so hot that electron-electron scattering can become significant. Thus, microscale heat transfer requires consideration of the microscopic energy carriers and the full range of possible scattering mechanisms.

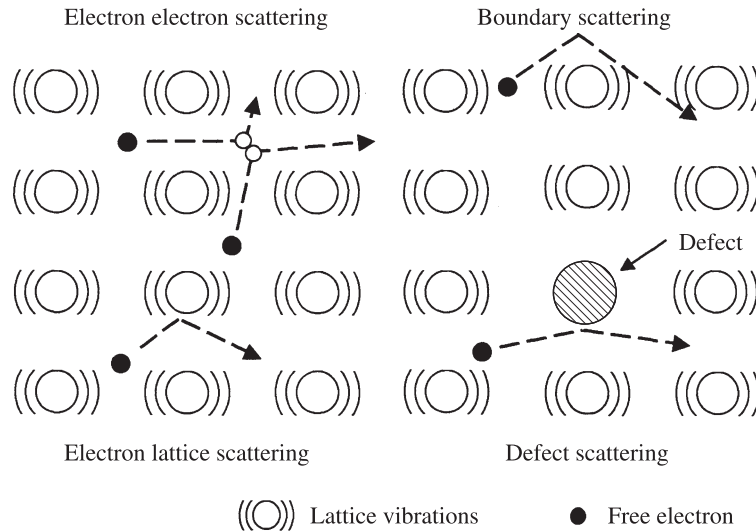


Figure 18.1 Primary scattering mechanisms of free electrons within a metal.

In the first section of this chapter we focus on defining and describing the microscopic heat carriers. The free electrons are typically responsible for thermal transport in metals. The governing statistical distribution is presented and discussed, along with equations for thermal conduction and the electron heat capacity. In an insulating material, thermal transport is accomplished through the motion of lattice vibrations called *phonons*. These lattice vibrations or phonons are discussed in detail. The primary heat carriers in semiconductor materials are also phonons, and therefore the thermal transport properties of semiconductors are determined in the same manner as for insulating materials. The formulations for these energy carriers are then used to explain and calculate the phonon thermal conductivity and lattice heat capacity of crystalline materials.

Experimental observation and measurement of microscale thermophysical properties is the subject of the next section. These techniques can be either steady-state, modulated, or pulsed transient techniques. Steady-state techniques typically focus on measuring the surface temperature with high spatial resolution, while the transient techniques are better suited for measuring transport properties on microscopic length scales. The majority of these techniques utilize either one or more of the following methods for determining thermal effects; nanoscale thermocouples, the temperature dependence of the electrical resistance of a microbridge, or thermal effects on the refractive index monitored using optical techniques. Three common methods for measuring microscale thermal phenomena are discussed in more detail.

In the final section we focus on specific applications where consideration of microscale heat transfer is important. For example, the microelectronics industry is perpetually looking for materials with lower dielectric constants to keep pace with the

miniaturization trend. Unfortunately, materials that are good electrical insulators are typically also good thermal insulators. As another example, high-power diode lasers and, particularly, vertical cavity surface-emitting laser diodes are often limited by the dissipation of thermal energy. These devices are an example of the increased trend toward multilayer thin-film structures. Recently, developers of thermoelectric materials have been using multilayer superlattice structures to reduce thermal transport normal to the material. This could significantly increase the efficiency of thermoelectric coolers. These examples represent just a few areas in which advancements in nanotechnology will have a dramatic impact on our lives.

18.2 MICROSCOPIC DESCRIPTION OF SOLIDS

To proceed with a discussion of microscale heat transfer, it is necessary first to examine the microscopic energy carriers and the basic heat transfer mechanisms. In metals, thermal transport occurs primarily from the motion of free electrons, while in semiconductors and insulators, thermal transport occurs due to lattice vibrations that travel about the material much like acoustic waves. In this chapter a conscious decision was made to minimize the presentation of quantum mechanical derivations and focus on a more physical presentation. More detailed descriptions of the material presented in this section can be found in most basic solid-state physics textbooks such as those of Ashcroft and Mermin (1976) and Kittel (1996). The theoretical descriptions of electrons and phonons usually include an assumption that the material has a crystalline structure. Therefore, this section begins with the basic relevant concepts of crystalline structures.

18.2.1 Crystalline Structure

The atoms within a solid structure arrange themselves in an organized manner such that the potential energy stored within the lattice is minimized. If the structure has long-range order, the material is referred to as *crystalline*. Once this structure is formed, smaller individual pieces of the crystalline can usually be identified that, when repeated in each direction, comprise the entire solid material. This type of material is then referred to as *single crystalline*. Most real materials contain grains, which are single crystalline; however, when the grains meet, a grain boundary is formed and the material is described as *polycrystalline*. In this section the assumption is made that the materials are single crystalline. However, the issues of grain size and boundaries, which arise in polycrystalline materials, are very important to the study of microscale heat transfer since the grain boundaries can scatter energy carriers and impede thermal transport.

The smallest of the individual structures that make up the entire crystal are called *unit cells*. Once the crystal has been broken down into unit cells, it must be determined whether the unit cells make up a *Bravais lattice*. Several criteria must be satisfied before a Bravais lattice can be identified. First, it must be possible to define a set of vectors, \mathbf{R} , which can describe the location of all points within the lattice,

$$\mathbf{R} = n_1 \mathbf{a}_1 + n_2 \mathbf{a}_2 + n_3 \mathbf{a}_3 \quad (18.1)$$

where n_1 , n_2 , and n_3 are integers. The set of primitive vectors \mathbf{a}_i are defined in the same manner. The three independent vectors \mathbf{a}_i can be used to translate between any of the lattice points using a linear combination of these vectors. Second, the structure of the lattice must appear exactly the same regardless of the point from which the array is viewed. Described in another way, if the lattice is observed from the perspective of an individual atom, all the surrounding atoms should appear to be identical, independent of which atom is chosen as the observation point.

There are 14 three-dimensional lattice types (Kittel, 1996). However, the most important are the *simple cubic* (SC), *face-centered cubic* (FCC), and *body-centered cubic* (BCC). These structures are Bravais lattices only when all the atoms are identical, as is the case with any element. When the atoms are different, these structures are not Bravais lattices. The NaCl structure is an example of a simple cubic structure, as shown in Fig. 18.2a, where the sodium and chloride atoms occupy alternating positions. For this structure to meet the criteria of a Bravais lattice, to be seen as identical regardless of the viewing point, the Na and Cl atoms must be grouped. Whenever two atoms are grouped, the lattice is said to have a *two-point basis*. In a Bravais lattice each unit cell contains only one atom, while each unit cell of a lattice with a two-point basis will contain the two grouped atoms. When each sodium atom is grouped with a chlorine atom, the result is a Bravais lattice with a two-point basis, shown in Fig. 18.2b by dark solid lines.

It is also possible to have a lattice with a basis even if all the atoms are identical; the most important crystal structure that falls into this category is the diamond structure. The group IV elements C, Si, Ge, and Sn can all have this structure. In addition, many III–V semiconductors, such as GaAs, also have the diamond structure. The diamond structure is a FCC Bravais lattice with a two-point basis, or equivalently, the diamond structure is composed of two offset FCC lattices.

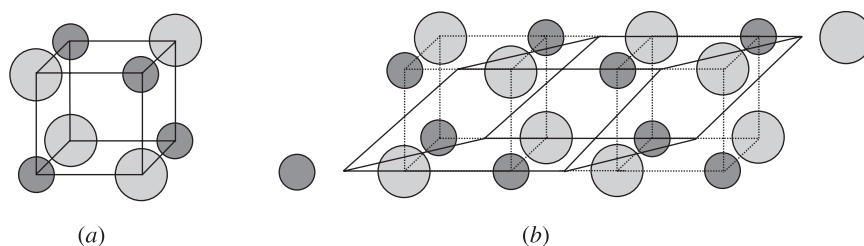


Figure 18.2 (a) NaCl structure shown as a simple cubic unit cell where the Na atom is the solid circle and the Cl atom is the shaded circle. (b) Each Na atom has been grouped with the Cl atom on its left, this pair of atoms form the two-point basis. The NaCl structure can then be arranged as a Bravais lattice using the two-point basis, where the unit cell is shown by the dark solid line.

For the purposes of understanding microscale heat transfer, there are two important concepts regarding crystalline structures that must be understood. The first is the concept of a Bravais lattice, which has just been presented. It is important in the study of energy transport on a microscale basis to know the Bravais lattice structure of the material of interest and whether or not the crystal is a lattice with a basis. The second important concept is the idea of the reciprocal lattice.

The structure of a crystal has an intrinsic periodicity that begins with the Bravais lattice unit cell. Certain properties, such as the electron density of the material, will vary between lattice sites but will vary periodically with the lattice. It is also common to be dealing with waves or particles with wavelike properties traveling within the crystal. In both cases, it is advantageous to define a *reciprocal lattice*. The set of all wave vectors \mathbf{k} , which represent plane waves with the periodicity of a given Bravais lattice, is described by the reciprocal lattice vectors. Given the Bravais lattice vector \mathbf{R} , the reciprocal lattice vectors can be defined as the set of vectors that satisfy the equation

$$e^{i\mathbf{k}\cdot(\mathbf{r}+\mathbf{R})} = e^{i\mathbf{k}\cdot\mathbf{r}} \quad (18.2)$$

where \mathbf{r} is any vector within the lattice. It can be shown that the reciprocal lattice of a Bravais lattice is also a Bravais lattice, which also has a set of primitive vectors \mathbf{b} . It turns out that the reciprocal lattice of a FCC lattice is a BCC lattice, the reciprocal lattice of a BCC lattice is FCC, and the reciprocal lattice of a SC lattice is still simple cubic.

Once the reciprocal lattice vectors have been defined, the *Brillouin zone* can be found. The Brillouin zone is a unit cell of the reciprocal lattice centered on a particular lattice site and containing all points that are closer to that lattice site than to any other lattice site. According to the definition of a Bravais lattice, if the Brillouin zone is drawn around each lattice point, the entire volume will be filled and each Brillouin zone will be identical. The manner in which the Brillouin zone is constructed geometrically is: (1) Draw lines from one reciprocal lattice site to all neighboring sites, (2) draw planes normal to each line that bisect the line, and (3) end each plane once it has intersected with another plane. The result is a choppy sphere that contains all the points closer to the central reciprocal lattice point than any other reciprocal lattice point. Three-dimensional representation of the Brillouin zone can be found in most solid-state physics texts (Kittel, 1996).

18.2.2 Energy Carriers

Thermal conduction through solid materials takes place both by the transport of vibrational energy within the lattice and by the motion of free electrons in a metal. In the next two sections a basic theoretical description of these energy carriers is presented. There are several significant differences in the behavior of these carriers that must be understood when dealing with microscale problems. There are also many similarities in the manner in which the problems are approached, despite the differences in the energy carriers.

18.2.3 Free Electron Gas

Many of the properties of metals can be explained adequately with the *free electron Fermi gas theory* (Ashcroft and Mermin, 1976). Although free electron gas theory does not adequately explain some properties, such as bandgaps in semiconductors, transport properties such as the electrical resistivity and thermal conductivity are well described by this theory. The assumption is made that each ion contributes a certain number of valence electrons to the Fermi gas and that these electrons are then free to move about the entire volume of the metal. The electron cloud is described appropriately as a gas, because any interactions other than collisions between electrons are neglected. Electron–electron collisions are usually negligible at or below room temperature, and electron collisions occur most frequently with the lattice, although scattering with defects, grain boundaries, and surfaces can also be significant.

Because the electrons have been assumed to be free and noninteracting, the allowable energy levels can be calculated using the free-particle Schrödinger equation. The allowable wavevectors in Cartesian coordinates that satisfy periodic boundary conditions in a three-dimensional cubic crystal, where the length of each side of the crystal is L , are found to be of the form

$$\mathbf{k}_x = \frac{2\pi n_x}{L} \quad \mathbf{k}_y = \frac{2\pi n_y}{L} \quad \mathbf{k}_z = \frac{2\pi n_z}{L} \quad (18.3)$$

where n_x , n_y , and n_z are integer quantities. The allowable energy levels can be expressed in terms of the electron wavevectors \mathbf{k} :

$$\varepsilon_{\mathbf{k}} = \frac{\hbar^2 \mathbf{k}^2}{2m} \quad (18.4)$$

where m is the effective mass of an electron and \hbar is Planck's constant. Each atom contributes a certain number of electrons to give a total number N_e of free electrons. According to the *Pauli exclusion principle*, no two electrons can occupy the same energy state. The electrons start filling energy levels beginning with the lowest energy level and the energy of the highest level that is occupied at zero temperature is called the *Fermi energy*.

The Fermi energy ε_F is often visualized as a sphere plotted as a function of wavevector \mathbf{k} , where the radius is given by the Fermi wavevector k_F , which is the wavevector of the highest occupied energy level. In theory, the surface of this sphere is not continuous, but rather, a collection of discrete wavevectors. However, because the value of N_e is usually very large, the assumption of a smooth sphere is typically reasonable. According to the Pauli exclusion principle, each electron must have a particular wavevector. However, since there are two spin states, there are two allowable energy levels for each wavevector. Thus, there must be $N_e/2$ wavevectors contained within the sphere. As shown in eq. (18.3), the linear distance between allowable wavevectors is $2\pi/L$. Therefore, the volume of each wavevector element in reciprocal space is $(2\pi/L)^3$ or $8\pi^3/V$. The number of wavevectors contained in the

sphere times the volume taken up by each wavevector must equal the volume of the sphere of radius k_F . Therefore, the Fermi wavevector can be calculated as

$$\frac{8\pi^3}{V} \frac{N_e}{2} = \frac{4}{3} \pi k_F^3 \rightarrow k_F = \left(\frac{3\pi^2 N_e}{V} \right)^{1/3} \quad (18.5)$$

which when substituted into eq. (18.4) yields an expression for the Fermi energy:

$$\varepsilon_F = \frac{\hbar^2 k_F^2}{2m} = \frac{\hbar^2}{2m} \left(\frac{3\pi^2 N_e}{V} \right)^{2/3} \quad (18.6)$$

where m is the effective mass of an electron and \hbar is Planck's constant.

Up to this point, the temperature of the electron gas has been assumed to be zero; therefore, all the energy levels up to the Fermi energy are occupied, whereas all energy levels above the Fermi energy are vacant. The occupational probability of a free electron gas as a function of temperature is given by the Fermi–Dirac distribution,

$$f(\varepsilon) = \frac{1}{e^{(\varepsilon - \mu)/k_B T} + 1} \quad (18.7)$$

where μ is the thermodynamic potential, k_B the Boltzmann constant, and T the temperature of the electron gas. The chemical potential μ is a function of temperature but can be approximated by the Fermi energy for temperatures at or below room temperature (Kittel, 1996).

Now that the allowable energy levels and the governing statistics have been defined for the free electron systems, it is possible to calculate the transport properties of the free electron systems. This was first done by Sommerfeld in 1928 using the Fermi–Dirac statistics (Wilson, 1954). However, in many instances it will be more convenient to integrate over energy states of the electron system rather than wavevectors. Therefore, the density of states $D(\varepsilon)$ is defined such that a single integration can be performed over the energy. The density of states can be determined by the following expression for the electron number density n_e :

$$n_e = \int \frac{1}{4\pi^3} f(\mathbf{k}) d\mathbf{k} = \int_0^\infty D(\varepsilon) f(\varepsilon) d\varepsilon \quad (18.8)$$

Using eq. (18.8), the electron density of states, which represents the number of available states of energy ε , can be calculated as

$$D(\varepsilon) = \frac{m}{\hbar^2 \pi^2} \sqrt{\frac{2m\varepsilon}{\hbar^2}} \quad (18.9)$$

where m is the effective mass of an electron. Once the density of states has been determined, the specific internal energy stored within the electron system can be found by

$$u_e = \int_0^\infty \varepsilon D(\varepsilon) f(\varepsilon) d\varepsilon \quad (18.10)$$

18.2.4 Vibrational Modes of a Crystal

In this section, the manner in which vibrational energy is transported through a crystalline lattice is discussed. For this discussion, the primary emphasis is on the positions of the ions within the lattice and the interatomic forces. Several assumptions are made at this point to simplify the analysis. The first is that the mean equilibrium position of each ion is about its assigned lattice site within the Bravais lattice given by the vector \mathbf{R} . The second is that the distance between the ion and the lattice site is much smaller than the interatomic spacing. Therefore, the position of each ion can be expressed in terms of the stationary Bravais lattice site and some displacement:

$$\mathbf{r}(\mathbf{R}) = \mathbf{R} + \mathbf{u}(\mathbf{R}) \quad (18.11)$$

Calculation of the vibrational modes in three dimensions is involved; therefore, the discussion will begin with the one-dimensional case. The observations that are made based on the one-dimensional model will generally hold true in a three-dimensional crystal. The analysis begins with a simple linear chain of atoms, shown in Fig. 18.3, where solid vertical lines give the positions of the equilibrium lattice sites. Their positions are given by an integer times a , the distance between lattice sites. The atoms are connected by springs, with spring constant K , that represent a linearization of the restoring forces that act between ions. The displacement u_n of each ion from the lattice is measured relative to the n th lattice site.

The equations of motion for the atoms within the system are given by the expression

$$M \frac{d^2 u_n}{dt^2} = K(u_{n+1} - 2u_n + u_{n-1}) \quad (18.12)$$

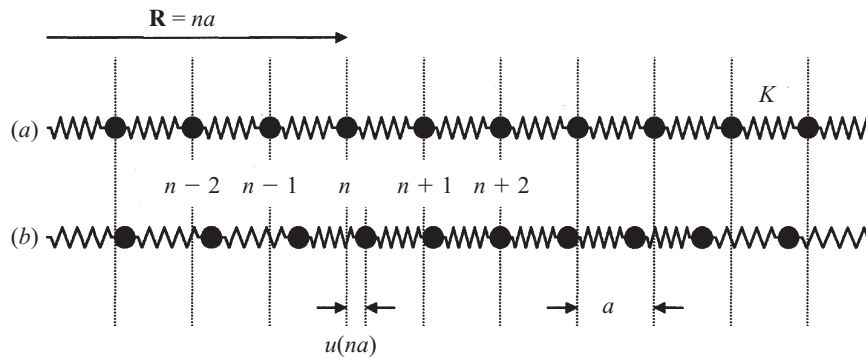


Figure 18.3 (a) Linear chain of atoms at their equilibrium lattice sites, $\mathbf{R} = na$; (b) linear chain of atoms where the individual atoms are displaced from their equilibrium positions by $u(na)$.

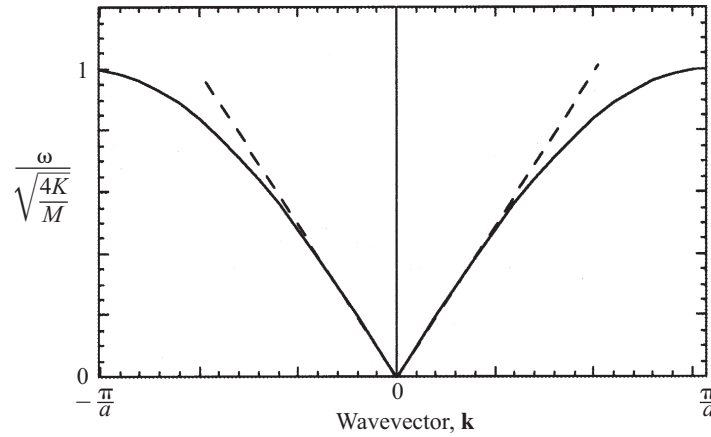


Figure 18.4 Plot of the frequency of a plane wave propagating in the crystal as a function of wavevector. Note that the relationship is linear until $\mathbf{k} \simeq 1/a$.

where M is the mass of an individual atom. By taking the time dependence of the solution to be of the form $\exp(-i\omega t)$, the frequency of the solution as a function of the wavevector can be determined as given by eq. (18.13). Figure 18.4 shows the results of this equation plotted over all the values that produce independent results. Values of \mathbf{k} larger than π/a correspond to plane waves with wavelengths less than the interatomic spacing. Because the atoms are located at discrete points, solutions to the equations above yielding wavelengths less than the interatomic spacing are not unique solutions, and these solutions can be equally well represented by long-wavelength solutions.

$$\omega(\mathbf{k}) = \sqrt{\frac{4K}{M}} \left| \sin \frac{1}{2} \mathbf{k}a \right| \quad (18.13)$$

The results shown in Fig. 18.4 apply for a Bravais lattice in one dimension, which can be represented by a linear chain of identical atoms connected by springs with the same spring constant, K . A Bravais lattice with a two-point basis can be represented in one dimension by either a linear chain of alternating masses M_1 and M_2 , separated by a constant spring constant K , or by a linear chain of constant masses M , with the spring constant of every other spring alternating between K_1 and K_2 . The theoretical results are similar in both cases, but only the case of a linear chain with atoms connected by two different springs, K_1 and K_2 , where the springs alternate between the atoms, is discussed. The results are shown in Fig. 18.5. The displacement of each atom from each equilibrium point is given by either $u(na)$ for atoms with the K_1 spring on their right and $v(na)$ for atoms with the K_1 spring on their left.

The reason for selecting this case is its similarity to the diamond structure. Recall that the diamond structure is a FCC Bravais lattice with a two-point basis; all the atoms are identical, but the spacing between atoms varies. As the distance varies

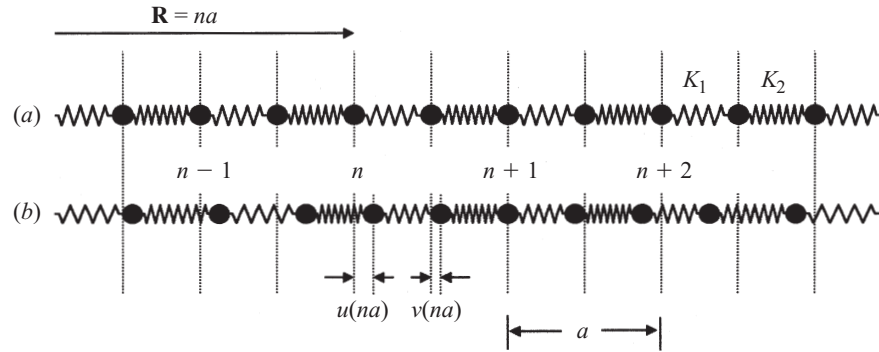


Figure 18.5 (a) One-dimensional Bravais lattice with two atoms per primitive cell shown in their equilibrium positions. The atoms are identical in mass; however, the atoms are connected by springs with alternating strengths K_1 and K_2 . (b) One-dimensional Bravais lattice with two atoms per primitive cell where the atoms are displaced by $u(na)$ and $v(na)$.

between atoms, so do the intermolecular forces, which are represented here by two different spring constants. The equations of motion for this system are given by

$$M \frac{d^2 u_n}{dt^2} = -K_1(u_n - v_n) - K_2(u_n - v_{n-1}) \quad (18.14a)$$

$$M \frac{d^2 v_n}{dt^2} = -K_1(v_n - u_n) - K_2(v_n - u_{n+1}) \quad (18.14b)$$

where u_n and v_n represent the displacement of the first and second atoms within the primitive cell, and K_1 and K_2 are the spring constants of the alternating springs. Again taking the time dependence of the solution to be of the form $e^{-i\omega t}$, the frequency of the solutions as a function of the wavevector can be determined as given by eq. (18.15) and shown in Fig. 18.6, assuming that $K_2 > K_1$:

$$\omega^2 = \frac{K_1 + K_2}{M} \pm \frac{1}{M} \sqrt{K_1^2 + K_2^2 + 2K_1 K_2 \cos \mathbf{k}a} \quad (18.15)$$

The expression relating the lattice vibrational frequency ω and wavevector \mathbf{k} is typically called the *dispersion relation*. There are several significant differences between the dispersion relation for a Bravais lattice without a basis [eq. (18.13)] versus a lattice with a basis [eq. (18.15)]. One of the most valuable pieces of information that can be gathered from the dispersion relation is the group velocity. The group velocity v_g governs the rate of energy transport within a material and is given by the expression

$$v_g = \frac{\partial \omega}{\partial \mathbf{k}} \quad (18.16)$$

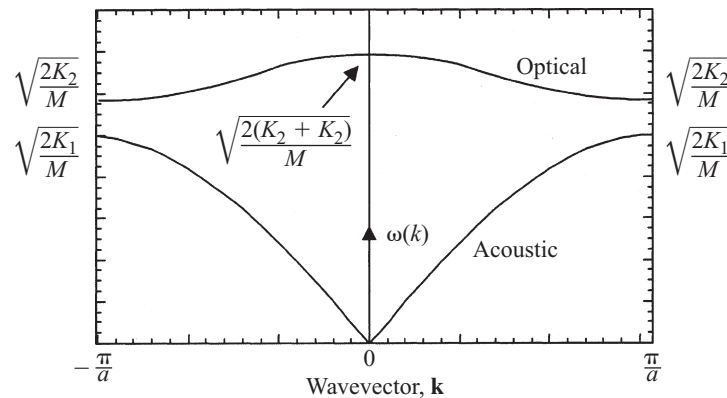


Figure 18.6 Dispersion relation for a one-dimensional Bravais lattice with a two-point basis.

The dispersion relations shown in Fig. 18.4 and in the lower curve in Fig. 18.6 are both roughly linear until $\mathbf{k} \simeq 1/a$, at which point the slope decreases and vanishes at the edge of the Brillouin zone, where $\mathbf{k} = \pi/a$. From these dispersion relations it can be observed that the group velocity stays constant for small values of \mathbf{k} and goes to zero at the edge of the Brillouin zone. It follows directly that waves with small values of \mathbf{k} , corresponding to longer wavelengths, contribute significantly to the transport of energy within the material. These curves represent the acoustic branch of the dispersion relation because plane waves with small \mathbf{k} , or long wavelength, obey a linear dispersion relation $\omega = c\mathbf{k}$, where c is the speed of sound or acoustic velocity.

The upper curve shown in Fig. 18.6 is commonly referred to as the *optical branch* of the dispersion relation. The name comes from the fact that the higher frequencies associated with these vibrational modes enable some interesting interactions with light at or near the visible spectrum. The group velocity of these waves is typically much less than for the acoustic branch. Therefore, contributions from the optical branch are usually considered negligible when evaluating the transport properties. Contributions from the optical branch must be considered when evaluating the specific heat.

Dispersion relations for a three-dimensional crystal in a particular direction will look very similar to one-dimensional relations except that there are transverse modes. The transverse modes arise due to the shear waves that can propagate in a three-dimensional crystal. The two transverse modes travel at velocities slower than the longitudinal mode; however, they still contribute to the transport properties. The optical branch can also have transverse modes. Again, optical branches occur only in three-dimensional Bravais lattices with a basis and do not contribute to the transport properties, due to their low group velocities.

Figure 18.7 shows the dispersion relations for lead at 100 K (Brockhouse et al., 1962). This is an example of a monoatomic Bravais lattice, since lead has a face-centered cubic (FCC) crystalline structure. Therefore, there are only acoustic branches, one longitudinal branch and two transverse. In the $[110]$ direction it is

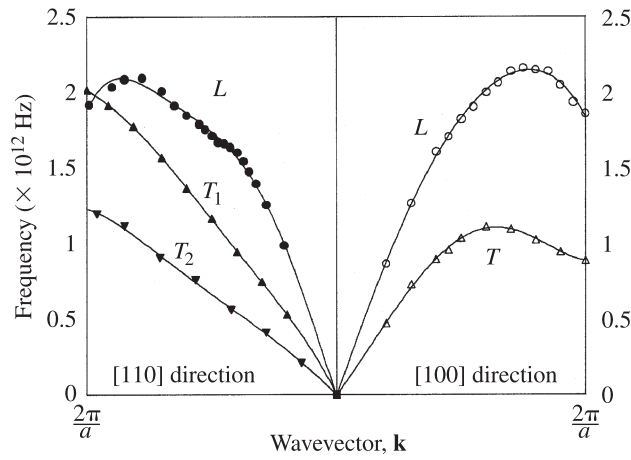


Figure 18.7 Dispersion relation for lead at 100 K plotted in the [110] and [100] directions. (From Brockhouse et al., 1962.)

possible to distinguish between the two transverse modes; however, due to the symmetry of the crystal, the two transverse modes happen to be identical in the [100] direction (Ashcroft and Mermin, 1976).

Finally, the concept of phonons must be introduced. The term *phonon* is commonly used in the study of the transport properties of the crystalline lattice. The definition of a phonon comes directly from the equation for the total internal energy U_l of a vibrating crystal:

$$U_l = \sum_{\mathbf{k}, s} \left[n_s(\mathbf{k}) + \frac{1}{2} \right] \hbar \omega(\mathbf{k}, s) \quad (18.17)$$

The simple explanation of eq. (18.17) is that the crystal can be seen as a collection of $3N$ simple harmonic oscillators, where N is the total number of atoms within the system and there are three modes of oscillation, one longitudinal and two transverse. Using quantum mechanics, one can derive the allowable energy levels for a simple harmonic oscillator, which is exactly the expression within the summation of eq. (18.17). The summation is taken over the allowable phonon wavevectors \mathbf{k} and the three modes of oscillation s . The definition of a phonon comes from the following statement: The integer quantity $n_s(\mathbf{k})$ is the mean number of phonons with energy $\hbar \omega(\mathbf{k}, s)$. Therefore, the number of phonons at a particular frequency simply represents the amplitude to which that vibrational mode is excited. Phonons obey the Bose–Einstein statistical distribution; therefore, the number of phonons with a particular frequency ω at an equilibrium temperature T is given by the equation

$$n_s(\mathbf{k}) = \frac{1}{e^{\hbar \omega(\mathbf{k}, s)/k_B T} - 1} \quad (18.18)$$

where k_B is the Boltzmann constant. Most thermal engineers are familiar with the concept of photons. Photons also obey the Bose–Einstein distribution; therefore, there are many conceptual similarities between phonons and photons.

The ability to calculate the energy stored within the lattice is important in any analysis of microscale heat transfer. Often, the calculations, which can be quite cumbersome, can be simplified by integrating over the allowable energy states. These integrations are actually performed over frequency, which is linearly related to energy through Planck's constant. The specific internal energy of the lattice, u_l , is then given by the equation

$$u_l = \sum_s \int D_s(\omega) n_s(\omega) \hbar \omega_s d\omega_s \quad (18.19)$$

where $D_s(\omega)$ is the phonon density of states, which is the number of phonon states with frequency between ω and $(\omega + d\omega)$ for each phonon branch designated by s . The actual density of states of a phonon system can be calculated from the measured dispersion relation; although often, simplifying assumptions are made for the density of states that will produce reasonable results.

18.2.5 Heat Capacity

The rate of thermal transport within a material is governed by the thermal diffusivity, which is the ratio of the thermal conductivity to the heat capacity. The heat capacity of a material is thus of critical importance to thermal performance. In this section the heat capacity of crystalline materials is examined. An understanding of the heat capacity of the different energy carriers, electrons and phonons, is important in the following section, where thermal conductivity is discussed. The heat capacity is defined as the change in internal energy of a material resulting from a change in temperature. The energy within a crystalline material, which is a function of temperature, is stored in the free electrons of a metal and within the lattice in the form of vibrational energy.

Electron Heat Capacity To solve for the electron heat capacity of a free electron metal, C_e , the derivative of the internal energy, stored within the electron system, is taken with respect to temperature:

$$C_e = \frac{\partial u_e}{\partial T} = \frac{\partial}{\partial T} \int_0^\infty \epsilon D(\epsilon) f(\epsilon) d\epsilon \quad (18.20)$$

The only temperature-dependent term within this integral is the Fermi–Dirac distribution. Therefore, the integral can be simplified, yielding an expression for the electron heat capacity:

$$C_e = \frac{\pi^2 k_B^2 n_e}{2\epsilon_F} T \quad (18.21)$$

where C_e is a linear function of temperature and n_e is the electron number density. The approximations made in the simplification of foregoing integral hold for electron temperatures above the melting point of the metal.

Phonon Heat Capacity Deriving an expression for the heat capacity of a crystal is slightly more complicated. Again, the derivative of the internal energy, stored within the vibrating lattice, is taken with respect to temperature:

$$C_l = \frac{\partial u_l}{\partial T} = \frac{\partial}{\partial T} \left[\sum_s \int D_s(\omega) n_s(\omega) \hbar \omega_s d\omega \right] \quad (18.22)$$

To calculate the lattice heat capacity, an expression for the phonon density of states is required. There are two common models for the density of states of the phonon system, the Debye model and the Einstein model. The *Debye model* assumes that all the phonons of a particular mode, longitudinal or transverse, have a linear dispersion relation. Because longer-wavelength phonons actually obey a linear dispersion relation, the Debye model predominantly captures the effects of the longer-wavelength phonons. In the *Einstein model*, all the phonons are assumed to have the same frequency and hence the dispersion relation is flat; this assumption is thus more representative of optical phonons. Because both optical and acoustic phonons contribute to the heat capacity, both models play a role in explaining the heat capacity. However, the acoustic phonons alone contribute to the transport properties; therefore, the Debye model will typically be used for calculating the transport properties.

Debye Model The basic assumption of the Debye model is that the dispersion relation is linear and all three acoustic branches have the speed of sound c :

$$\omega(\mathbf{k}) = c\mathbf{k} \quad (18.23)$$

However, unlike photons, this dispersion relation does not extend to infinity. Since there are only N primitive cells within the lattice, there are only N independent wavevectors for each acoustic mode. Using spherical coordinates again, conceive of a sphere of radius k_D in wavevector space, where the total number of allowable wavevectors within the sphere must be N and each individual wavevector occupies a volume of $(2\pi/L)^3$:

$$\frac{4}{3} \pi k_D^3 = N \left(\frac{2\pi}{L} \right)^3 \rightarrow k_D = \left(\frac{6\pi^2 N}{V} \right)^{1/3} \quad (18.24)$$

Using eq. (18.24), the maximum frequency allowed by the Debye model, known as the *Debye cutoff frequency* ω_D , is

$$\omega_D = c \left(\frac{6\pi^2 N}{V} \right)^{1/3} \quad (18.25)$$

Now that the maximum frequency allowed by the Debye model is known and it is assumed that the dispersion relation is linear, an expression for the phonon density of states is required. Again, the concept of a sphere in wavevector space can be used to find the number of allowable phonon modes N with wavevector less than k . Each allowable wavevector occupies a volume in reciprocal space equal to $(2\pi/L)^3$.

Therefore, the total volume of the sphere of radius k must be equal to the number of phonon modes with wavevector less than k multiplied times $(2\pi/L)^3$:

$$\frac{4}{3}\pi k^3 = N \left(\frac{2\pi}{L} \right)^3 \rightarrow N = \frac{V}{6\pi^2} k^3 \quad (18.26)$$

The phonon density of states $D(\omega)$ is the number of allowable states at a particular frequency and can be determined by the expression

$$D(\omega) = \frac{\partial N}{\partial \omega} = \frac{V}{2\pi^2 c^3} \omega^2 \quad (18.27)$$

Returning to eq. (18.22), all the information needed to calculate the lattice heat capacity is known. Again simplifying the problem by assuming that all three acoustic modes obey the same dispersion relation, $\omega(\mathbf{k}) = c\mathbf{k}$, the lattice heat capacity can be calculated using

$$C_l(T) = \frac{3V\hbar^2}{2\pi^2 c^3 k_B T^2} \int_0^{\omega_D} \omega^4 \frac{e^{\hbar\omega/k_B T}}{(e^{\hbar\omega/k_B T} - 1)^2} d\omega \quad (18.28)$$

which can be simplified further by introducing a term called the *Debye temperature*, θ_D . The Debye temperature is calculated directly from the Debye cutoff frequency,

$$k_B \theta_D = \hbar \omega_D \rightarrow \theta_D = \frac{\hbar \omega_D}{k_B} \quad (18.29)$$

With this new quantity, the lattice specific heat calculated under the assumptions of the Debye model can be expressed as

$$C_l(T) = 9Nk_B \left(\frac{T}{\theta_D} \right)^3 \int_0^{\theta_D/T} \frac{x^4 e^x}{(e^x - 1)^2} dx \quad (18.30)$$

Figure 18.8 shows the molar values of the specific heat of Au compared to the results of eq. (18.30) using a Debye temperature of 170 K. Although a theoretical value of the Debye temperature can be calculated using eq. (18.29), the published values are typically determined by comparing the theoretical predictions to the measured values.

The low-temperature specific heat is important in analysis of the lattice thermal conductivity. If the temperature is much less than the Debye temperature, the lattice heat capacity is proportional to T^3 . This proportionality is easily seen in Fig. 18.9, where the information contained in Fig. 18.8 is plotted on a logarithmic plot to highlight the exponential dependence on temperature. The Debye model accurately predicts this T^3 dependence.

Einstein Model The Einstein model for the phonon density of states is based on the assumption that the dispersion relation is flat. In other words, the assumption is

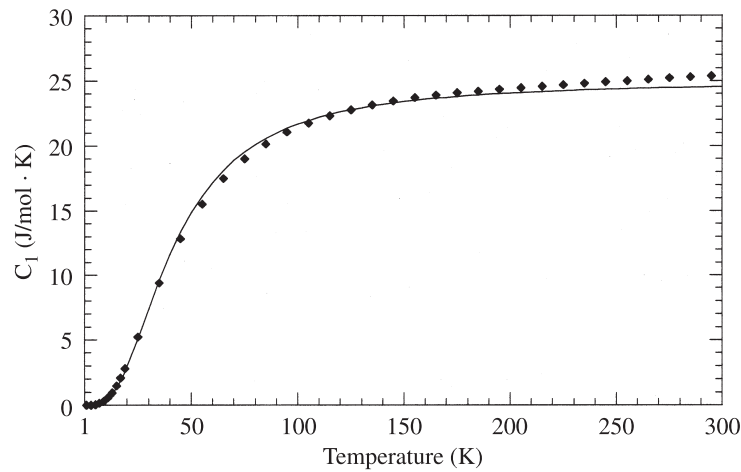


Figure 18.8 Molar specific heat of Au compared to the Debye model (eq. 18.30) using 170 K for the Debye temperature. (From Weast et al., 1985.)

made that all N simple harmonic oscillators are vibrating at the same frequency, ω_0 ; therefore, the density of states can be written as

$$D(\omega) = N\delta(\omega - \omega_0) \quad (18.31)$$

The method for calculating the heat capacity is exactly the same as that followed with the Debye model, although the integrals are simpler, due to the delta function.

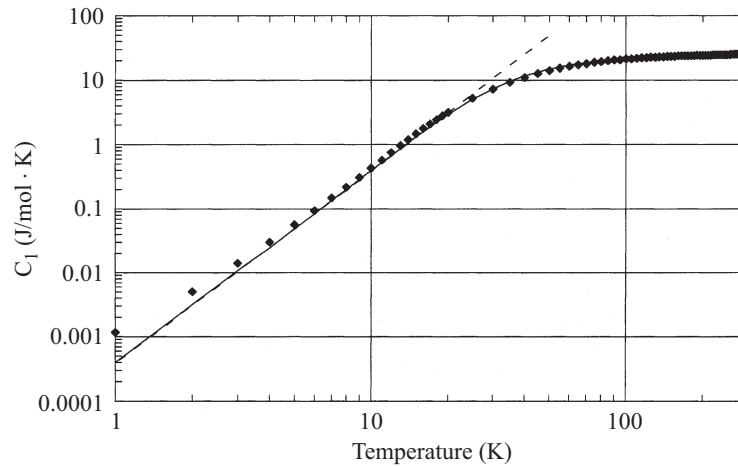


Figure 18.9 The T^3 dependence of the lattice specific heat is very apparent on a logarithmic plot of the molar specific heat of Au (Weast et al., 1985), compared to the Debye model (eq. 18.30) using 170 K for the Debye temperature.

This model provides better results than the Debye model for elements with the diamond structure. One reason for the improvement is the optical phonons in these materials. Optical phonons have a roughly flat dispersion relation, which is better represented by the Einstein model.

18.2.6 Thermal Conductivity

The specific energy carriers have been discussed in previous sections. The manner in which these carriers store energy, and the appropriate statistics that describe the energy levels that they occupy, have been presented. In the next section we focus on how these carriers transport energy and the mechanisms that inhibit the flow of thermal energy. Using very simple arguments from the kinetic theory of gases, an expression for the thermal conductivity K can be obtained:

$$K = \frac{1}{3} C v l \quad (18.32)$$

where C is the heat capacity of the particle, v the average velocity of the particles, and l the mean free path or average distance between collisions.

Electron Thermal Conductivity in Metals Thermal conduction within metals occurs due to the motion of free electrons within the metal. According to eq. (18.32), there are three factors that govern thermal conduction: the heat capacity of the energy carrier, the average velocity, and the mean free path. As shown in eq. (18.21), the electron heat capacity is linearly related to temperature. As for the velocity of the electrons, the Fermi–Dirac distribution, eq. (18.7), dictates that the only electrons within a metal that are able to undergo transitions, and thereby transport energy, are those located at energy levels near the Fermi energy. The energy contained within the electron system is purely kinetic and can therefore be converted into velocity. Because all electrons involved in transport of energy have an amount of kinetic energy close to the Fermi energy, they are all traveling at velocities near the Fermi velocity. Therefore, the assumption is made that all the electrons within the metal are traveling at the Fermi velocity, which is given by

$$v_F = \sqrt{\frac{2}{m} \varepsilon_F} \quad (18.33)$$

The third important contributor to the thermal conductivity is the electron mean free path, obviously a direct function of the electron collisional frequency. Electron collisions can occur with other electrons, the lattice, defects, grain boundaries, and surfaces. Assuming that each scattering mechanism is independent, *Matthiessen's rule* states that the total collisional rate is simply the sum of the individual scattering mechanisms (Ziman, 1960):

$$\nu_{\text{tot}} = \nu_{ee} + \nu_{ep} + \nu_d + \nu_b \quad (18.34)$$

where ν_{ee} is the electron–electron collisional frequency, ν_{ep} the electron–lattice collisional frequency, ν_d the electron–defect collisional frequency, and ν_b the electron–boundary collisional frequency. Consideration of each of these scattering mechanisms is important in the area of microscale heat transfer.

The temperature dependence of the collisional frequency can also be very important. Electron–defect and electron–boundary scattering are both typically independent of temperature, whereas for temperatures above the Debye temperature, the electron–lattice collisional frequency is proportional to the lattice temperature. Electron–electron scattering is proportional to the square of the electron temperature:

$$\nu_{ee} \simeq AT_e^2 \quad \nu_{ep} = BT_l \quad (18.35)$$

where A and B are constant coefficients and T_e and T_l are the electron and lattice temperatures. In clean samples at low temperatures, electron–lattice scattering dominates. However, electron–lattice scattering occurs much less frequently than simple kinetic theory would predict. In very pure samples and at very low temperatures, the mean free path of an electron can be as long as several centimeters, which is more than 10^8 times the distance between lattice sites. This is because the electrons do not scatter directly off the ions, due to the wavelike nature that allows the electrons to travel freely within the periodic structure of the lattice. Scattering occurs only when there are disturbances in the periodic structure of the lattice.

The temperature dependence of the thermal conductivity often allows us to isolate effects from several different mechanisms that affect the thermal conductivity. Figure 18.10 shows the thermal conductivity of three metals commonly used in the microelectronics industry: Cu, Al, and W. The general temperature dependence of all three metals is very similar. At very low temperatures, below 10 K, the primary

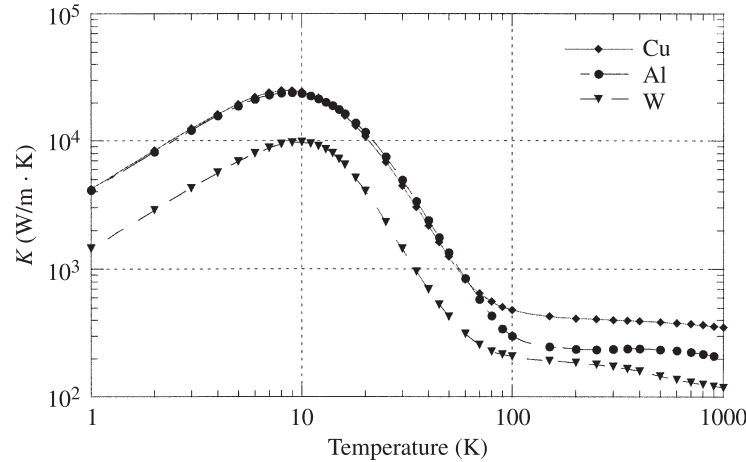


Figure 18.10 Thermal conductivity of Cu, Al, and W plotted as a function of temperature. (From Powell et al., 1966.)

scattering mechanism is due to either defect or boundary scattering, both of which are independent of temperature. The linear relation between the thermal conductivity and temperature in this regime arises from the linear temperature dependence of the electron heat capacity. At temperatures above the Debye temperature, the thermal conductivity is roughly independent of temperature as a result of competing temperature effects. The electron heat capacity is still linearly increasing with temperature [eq. (18.21)], but the mean free path is inversely proportional to temperature, due to increased electron–lattice collisions, as indicated by eq. (18.35).

Lattice Thermal Conductivity Thermal conduction within the crystalline lattice is due primarily to acoustic phonons. The original definition of phonons was based on the amplitude of a particular vibrational mode and that the energy contained within a phonon was finite. In this section, phonons are treated as particles, which is analogous to assuming that the phonon is a localized wave packet. Acoustic phonons generally follow a linear dispersion relation; therefore, the Debye model will generally be adopted when modeling the thermal transport properties, and the group velocity is assumed constant and equal to the speed of sound within the material. Thus, all the phonons are assumed to be traveling at a velocity equal to the speed of sound, which is independent of temperature. At very low temperatures the phonon heat capacity is proportional to T^3 , while at temperatures above the Debye temperature, the heat capacity is nearly constant.

The kinetic theory equation for the thermal conductivity of a diffusive system, eq. (18.32), is also very useful for understanding conduction in a phonon system. However, for this equation to be applicable, the phonons must scatter with each other, defects, and boundaries. If these interactions did not occur, the transport would be more radiative in nature. In some problems of interest in microscale heat transfer, the dimensions of the system are small enough that this is actually the case, and for these problems a model was developed called the *equations of phonon radiative transport* (Majumdar, 1993). However, in bulk materials, the phonons do scatter and the transport is diffusive. The phonons travel through the system much like waves, so it is easy to envision reflection and scattering occurring when waves encounter a change in the elastic properties of the material. Boundaries and defects obviously represent changes in the elastic properties. The manner in which scattering occurs between phonons is not as straightforward.

Two types of phonon–phonon collisions occur within crystals, described by either the *normal* or *N process* or the *Umklapp* or *U process*. In the simplest case, two phonons with wavevectors \mathbf{k}_1 and \mathbf{k}_2 collide and combine to form a third phonon with wavevector \mathbf{k}_3 . This collision must conserve energy:

$$\hbar\omega(\mathbf{k}_1) + \hbar\omega(\mathbf{k}_2) = \hbar\omega(\mathbf{k}_3) \quad (18.36)$$

Previously, the reciprocal lattice vector was defined as a vector through which any periodic property can be translated and still result in the same value. Since the dispersion relation is periodic throughout the reciprocal lattice,

$$\hbar\omega(\mathbf{k}) = \hbar\omega(\mathbf{k} + \mathbf{b}) \quad (18.37)$$

can be written. Here, \mathbf{b} is the reciprocal lattice vector. If eq. (18.37) is substituted into eq. (18.36) and a linear dispersion relation is assumed, $\omega(\mathbf{k}) = c\mathbf{k}$, then

$$\mathbf{k}_1 + \mathbf{k}_2 = \mathbf{k}_3 + \mathbf{b} \quad (18.38)$$

This equation is often referred to as the *conservation of quasi-momentum*, where $\hbar\mathbf{k}$ represents the phonon momentum. If $\mathbf{b} = 0$, the collision is called a normal or N process, and if $\mathbf{b} \neq 0$, the process is referred to as an Umklapp or U process. Examples of normal and Umklapp processes in one dimension are shown in Fig. 18.11.

The importance of distinguishing between N processes and U processes becomes apparent at low temperatures. At low temperatures, only long-wavelength phonons are excited, and these phonons have small wavevectors. Therefore, only normal scattering processes occur at low temperatures. Normal processes do not contribute to thermal resistance; therefore, phonon–phonon collisions do not contribute to low-temperature thermal conductivity. For higher temperatures, above the Debye temperature, however, all allowable modes of vibration are excited and the overall phonon population increases with temperature. Therefore, the frequency of U processes increases with increasing temperatures. This is the case for high temperatures, $T > \theta_D$, where the mean free path l_{pp} is inversely proportional to temperature:

$$l_{pp} \propto \frac{1}{T} \quad (18.39)$$

Figure 18.12 shows the thermal conductivity of three elements, all of which have the diamond structure and all of which exhibit the same general trend of thermal conductivity. At low temperatures, the normal processes do not affect the thermal conductivity. Defect and boundary scattering are independent of temperature; therefore, the temperature dependence arises from the heat capacity and follows the expected T^3 behavior. As the temperature increases, the heat capacity becomes constant, while the mean free path decreases, resulting in the approximately T^1 behavior at higher temperatures.

The thermal conductivity of crystalline SiO_2 , quartz, is shown in Fig. 18.13. The thermal conductivity has the same T^3 behavior at low temperature and T^1 behavior at

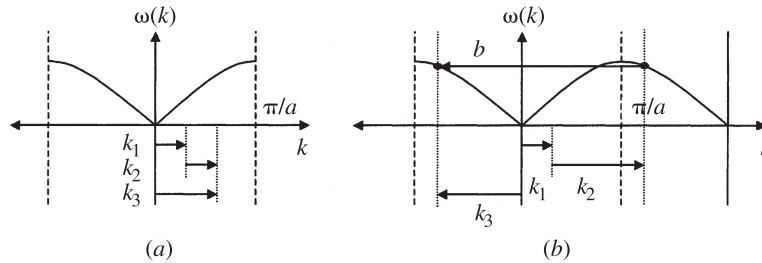


Figure 18.11 (a) Normal process where two phonons collide and the resulting phonon still resides within the Brillouin zone. (b) Umklapp process where two phonons collide and the resulting wavevector must be translated by the reciprocal lattice vector \mathbf{b} to remain within the original Brillouin zone.

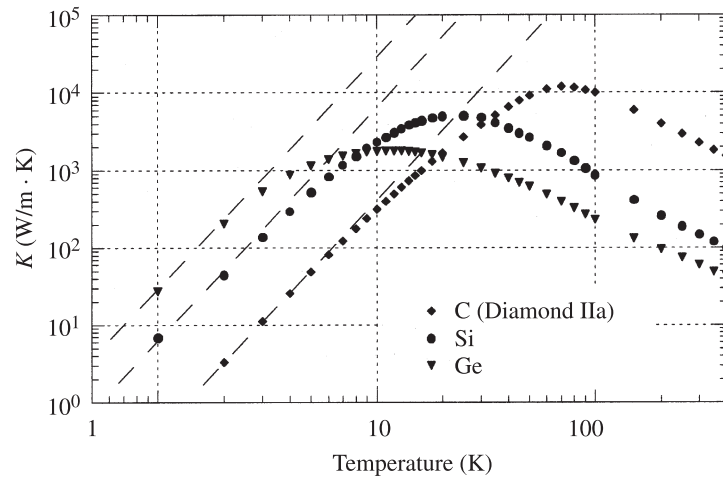


Figure 18.12 Thermal conductivity of the diamond structure shown as a function of temperature. (From Powell et al., 1974.)

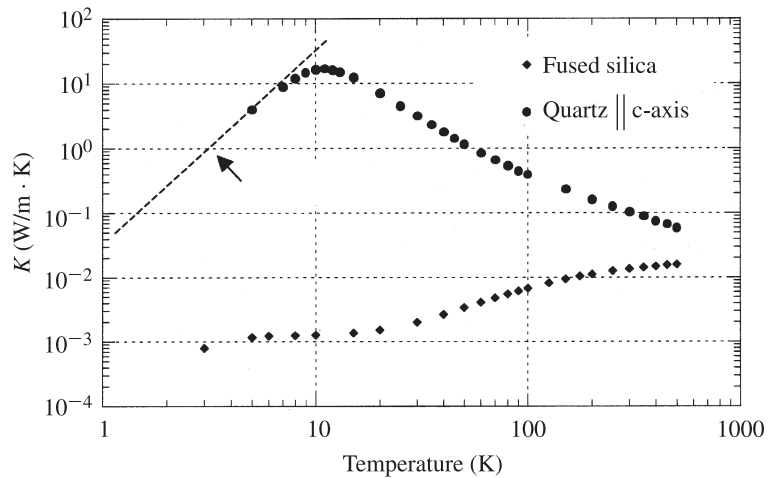


Figure 18.13 Thermal conductivity of crystalline and amorphous forms of SiO_2 . (From Powell et al., 1966.)

high temperature. The thermal conductivity is plotted for the direction parallel to the c -axis because quartz has a hexagonal crystalline structure. The thermal conductivity of fused silica, also shown in Fig. 18.13, does not follow this behavior since it is an amorphous material and does not have a crystalline structure. The thermal conductivity of amorphous materials is an entirely different subject, and the reader is referred to several good references on the subject, such as Cahill and Pohl (1988) and Mott (1993).

18.3 MODELING

Now that an understanding of the basic energy, carriers and the statistical procedures for dealing with these carriers has been developed, in this section we focus on a discussion of the methods for modeling heat transfer on the microscale. The first and simplest approach is to modify the continuum models to incorporate microscale heat transfer effects. Typically, continuum models can be used as long as meaningful local temperatures can be established. The next approach is to make use of the Boltzmann transport equation (Majumdar, 1998). With this approach, the transport equations developed are no longer dependent on temperature but on the statistical distributions of the energy carriers. The collisional term in the Boltzmann transport equation, however, is very difficult to model, and the assumptions made when modeling this term eventually limit the accuracy of this approach. Finally, the transport of thermal energy can be modeled using more molecular approaches, such as lattice dynamics, molecular dynamics, and Monte Carlo simulations (Klistner et al., 1988; Chou et al., 1999; Tamura et al., 1999). These approaches are the most fundamental in concept; however, they are computationally difficult and are ultimately limited by knowledge of the intermolecular forces between the atoms.

18.3.1 Continuum Models

Microscale heat transfer continuum models can be separated in several categories, depending on the basic transport mechanisms and the type of energy carriers involved. The first distinction is based on the manner in which heat transport occurs. If the energy carrier undergoes frequent collisions, transport is diffusive and the heat flux q is given by Fourier's law:

$$q = -K \nabla T \quad (18.40)$$

where K is the thermal conductivity. When eq. (18.40) is combined with the conservation of energy equation, the result is a parabolic differential equation. One theoretical problem with Fourier's law is that it yields an infinite speed of propagation of thermal energy. In other words, if the surface of a material is instantaneously heated, Fourier's law dictates that the thermal effect is felt immediately throughout the entire system. Typically, this effect is extremely small, and the speed with which the average of the thermal energy density travels is actually quite slow. Consider the one-dimensional heat equation for an instantaneous pulse that arrives at the surface at time zero:

$$C \frac{\partial T}{\partial t}(x, t) = \frac{\partial}{\partial x}(q) + S_o \delta(x) \delta(t) \quad (18.41)$$

where C is the heat capacity of the material, x the direction of heat flow, S_o the amount of energy deposited, and δ is a delta function. The solution to this problem is given by (Kittel and Kroemer, 1980)

$$T(x, t) = \frac{2S_o}{C} \sqrt{4\pi Dt} \exp\left(\frac{-x^2}{4Dt}\right) \quad (18.42)$$

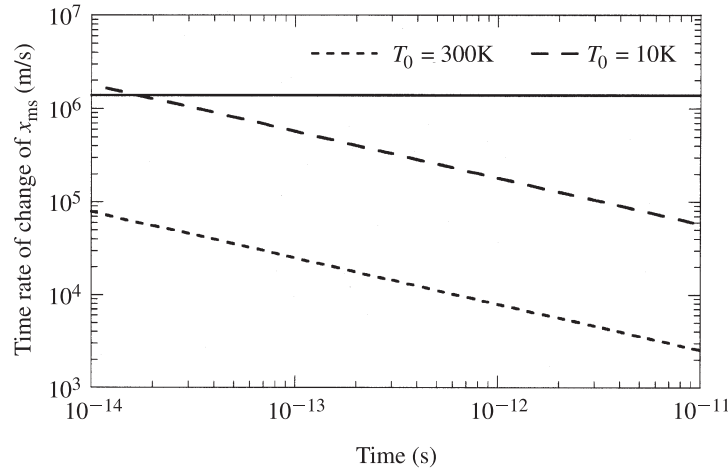


Figure 18.14 Time rate of change of the root mean square of the distance to which the effects of the instantaneous pulse have propagated plotted as a function of time.

where D is the thermal diffusivity of the material. The root mean square of the distance to which the effects of the instantaneous pulse have propagated is given by

$$x_{\text{rms}}(t) = \sqrt{2Dt} \quad (18.43)$$

Taking the derivative of this expression yields the average velocity with which the thermal energy propagates. Figure 18.14 shows the time rate of change of x_{rms} plotted versus time for Au at two different temperatures. In the low-temperature case, the time rate of change of x_{rms} , which represents the velocity of the energy carriers, exceeds the Fermi velocity for the first several hundred picoseconds. It is not possible for the thermal energy to propagate at this rate because the Fermi velocity represents the speed of the electrons. This illustrates that a time scale exists where a finite speed of propagation must be considered.

Cattaneo's equation was introduced to account for the finite speed of thermal energy propagation (Joseph and Preziosi, 1989). Essentially, Cattaneo's equation accounts for the time required for the heat flux to develop after a temperature gradient has been applied and is given by

$$\frac{1}{\tau} \frac{\partial q}{\partial t} + q = -K \nabla T \quad (18.44)$$

where τ is the relaxation time of the heat carrier. When this heat flux equation is combined with the conservation of energy equation, the result is a hyperbolic differential equation. This equation reduces to Fourier's law when the relaxation time is much less than the time scale of interest.

Another manner in which continuum thermal models have been modified to account for microscale heat transfer phenomena deals with equilibrium versus nonequilibrium systems. There are instances when multiple energy carriers may be involved

in a problem, and the representative temperature of each energy carrier system is different. Ultrashort pulsed laser heating and nonequilibrium Joule heating in field-effect transistors are two examples where nonequilibrium thermal systems occur. During ultrashort pulsed laser heating of metals, the electron and phonon systems can be treated separately. The conservation of energy equations for both systems are given by

$$C_e(T_e) \frac{\partial T_e}{\partial t} = \nabla(q_e) + G(T_e - T_l) + S_e \quad (18.45a)$$

$$C_l(T_l) \frac{\partial T_l}{\partial t} = \nabla(q_l) - G(T_e - T_l) + S_l \quad (18.45b)$$

where $G(T_e - T_l)$ is the rate of energy exchange between the two systems, G the electron–phonon coupling factor, and S_e and S_l are the source terms for the electron and lattice systems, respectively. The resulting system of equations can again be parabolic or hyperbolic, depending on the appropriate equation for the heat flux, eq. (18.40) or (18.44).

Even when continuum heat transfer equations are appropriate, the thermophysical properties can be influenced by microscale phenomena. The thermal conductivity can be reduced significantly due to increased defect and/or grain boundary scattering (Mayadas et al., 1969). When the length scale of the film is on the order of the heat carrier mean free path, there can be changes in the transport properties due to increased boundary scattering (Fuchs, 1938).

18.3.2 Boltzmann Transport Equation

The Boltzmann transport equation (BTE) is simply a conservation equation, where the conserved quantity is the number of particles. The general form of the BTE is given by the following equation for classical particles (Ziman, 1960):

$$\underbrace{\frac{\partial}{\partial t} [f(\mathbf{x}, \mathbf{P}, t) dV_x dV_P]}_{\text{total time rate of change of number of particles}} + \underbrace{\mathbf{v} \cdot \nabla_x [f(\mathbf{x}, \mathbf{P}, t) dV_x dV_P]}_{\text{convection of particles in physical space}} + \underbrace{\mathbf{F} \cdot \nabla_P [f(\mathbf{x}, \mathbf{P}, t) dV_x dV_P]}_{\text{convection of particles in momentum space}} = \underbrace{\left\{ \frac{\partial}{\partial t} [f(\mathbf{x}, \mathbf{P}, t) dV_x dV_P] \right\}_{\text{coll}}}_{\text{time rate of change of number of particles due to collisions}} \quad (18.46)$$

where f is the distribution of particles, dV_x a differential control volume located at position x , and dV_P a differential control volume located at momentum P . The first term represents the quantity of interest, the time rate of change of the number of particles at position x that have velocity v . The second term represents particles

that physically cross the boundaries of the differential control volume in physical space. The third term accounts for particles that are acted on by an external force F and are therefore accelerated into or out of the differential control volume in velocity space. Finally, the right-hand side of the equation accounts for changes in position and velocity which can occur whenever two particles collide. This equation is directly applicable to electrons and classical particles where the momentum is represented by $\mathbf{P} = m\mathbf{v}$. In the case of electrons, the momentum can be expressed in terms of the wavevector using the expression $\mathbf{P} = \hbar\mathbf{k}$. This equation for the momentum is also used with phonons and photons; however, momentum is not strictly conserved, eq. (18.38).

When applying eq. (18.46) in the solution of microscale heat transfer problems, the greatest difficulty comes from the collisional term on the right-hand side. General expressions for the collisional frequencies of electron–electron, electron–phonon, and phonon–phonon scattering have already been presented as eqs. (18.35) and (18.39). However, the detailed nature of these collisions has not been examined fully. Typically, the relaxation time approximation is utilized. Under this approximation, the following expression is used:

$$\left(\frac{\partial f}{\partial t}\right)_{\text{collisions}} = -\frac{f - f_o}{\tau} \quad (18.47)$$

where f_o is the equilibrium distribution and τ is the relaxation time. The relaxation time approximation is based on the assumption of a distribution that is slightly perturbed from its equilibrium distribution f such that the distribution function can be written as $f = f_o + f'$. Collisions within the system will then act to bring about an equilibrium distribution. Substituting this expression into eq. (18.47) and solving for the deviation from equilibrium as a function of time due solely to collisional effects yields

$$\frac{\partial f'}{\partial t} = -\frac{f'}{\tau} \rightarrow f'(t) = e^{t/\tau} \quad (18.48)$$

Therefore, by using eq. (18.47) for the collisional term, the assumption has been made that the collisions within the system will bring any deviation back to equilibrium according to an exponential decay. The relaxation time τ is simply the time required for the collisional effects to decrease the deviation by a factor of $1/e$. Although the relaxation time is not exactly the mean free time between collisions, the two are often assumed to be of the same order of magnitude and will sometimes be used interchangeably. When multiple relaxation times are applicable, such as electron–lattice and electron–defect scattering, they may be combined by again using Mathiessen's rule, eq. (18.34), assuming that the collisional mechanisms are independent. Note that the relaxation time is inversely proportional to the collisional frequency.

Phonons A general form of the Boltzmann transport equation for a phonon system is given by

$$\begin{aligned} \frac{\partial}{\partial t} [N(\mathbf{x}, \mathbf{k}, t) dV_x dV_k] + \mathbf{v} \cdot \nabla_x [N(\mathbf{x}, \mathbf{k}, t) dV_x dV_k] \\ = - \left(\frac{N(\mathbf{x}, \mathbf{k}, t) - N_o(\mathbf{x}, \mathbf{k}, t)}{\tau} \right) \end{aligned} \quad (18.49)$$

where $N(\mathbf{x}, \mathbf{k}, t)$ is the Bose-Einstein distribution as a function of position, wavevector, and time, and $\hbar \mathbf{k}$ is used to express the quasi-momentum of the phonon. The assumption is made that no external forces act on the phonons within the crystal. Using this form, the rate of heat transfer due to phonons can be determined within a crystal under a steady-state temperature gradient applied in the x direction. The one-dimensional Boltzmann transport equation can be written as

$$v_x \frac{\partial N}{\partial x} = - \frac{N - N_o}{\tau} \quad (18.50)$$

Thermal transport within the crystal occurs due to slight deviations from an equilibrium distribution, $N = N_o + N$. The assumption that $\partial N_o / \partial x \gg \partial N / \partial x$ yields

$$N = -v_x \tau \frac{\partial N_o}{\partial x} \quad (18.51)$$

Because the equilibrium distribution does not contribute to heat flux, f' yields the only contribution. The heat flux of a phonon system can be written in terms of the number of electrons traveling in the x direction carrying energy $\hbar \omega$:

$$q_x = \int v_x N(\omega) \hbar \omega D(\omega) d\omega \quad (18.52)$$

where $D(\omega)$ is the phonon density of states. Substituting the expression for N given in eq. (18.51) into eq. (18.52) yields

$$q_x = \begin{cases} \int v_x \left(-v_x \tau \frac{\partial N_o}{\partial x} \right) \hbar \omega D(\omega) d\omega & (18.53a) \\ \int v_x \left(-v_x \tau \frac{\partial N_o}{\partial T} \frac{\partial T}{\partial x} \right) \hbar \omega D(\omega) d\omega & (18.53b) \\ -v_x^2 \tau \left[\int \frac{\partial N_o}{\partial T} \hbar \omega D(\omega) d\omega \right] \frac{dT}{dx} & (18.53c) \end{cases}$$

The expression inside the brackets in eq. (18.53c) is, by definition, the lattice heat capacity, eq. (18.22). The mean free path of a phonon is equal to the product of the mean free time between collisions and the speed of the particle, $\Lambda = v \tau_p$. The speed of sound in the solid is equal to the square root of the sum of the three velocity components squared. If all the velocity components are equal, $v_x = \frac{1}{3} v^2$. Substituting all these expressions into eq. (18.53c) gives the same expression for the thermal conductivity that was presented as eq. (18.32):

$$q_x = -\frac{1}{3}Cv\Lambda \frac{dT}{dx} \quad (18.54)$$

If the problem is transient rather than steady state, the time derivative term must be retained in the Boltzmann transport equation. Making the same assumptions as were made for the steady-state case, the BTE can be reduced to the form

$$\tau \frac{\partial f'}{\partial t} + f' = -v_x \tau \frac{\partial f_o}{\partial x} \quad (18.55)$$

This solution can then be used to derive an equation for the heat flux, which is identical to Catteneo's equation for hyperbolic heat conduction:

$$\tau \frac{\partial q}{\partial t} + q = -\frac{1}{3}Cv\Lambda \frac{\partial T}{\partial x} \quad (18.56)$$

Despite this result, experience indicates that Fourier's law is applicable for most transient problems. This is because in most heat transfer problems the time scale of interest is much larger than the relaxation time of the energy carrier, in which case the first term can be neglected.

Electrons When dealing with the transport properties of metals, such as current density and thermal conduction due to the electrons, it is useful to begin with the general form of the Boltzmann transport equation for an electron system as given by the expression

$$\begin{aligned} \frac{\partial}{\partial t} [f(\mathbf{x}, \mathbf{k}, t) dV_x dV_k] + \mathbf{v} \cdot \nabla_x [f(\mathbf{x}, \mathbf{k}, t) dV_x dV_k] - \frac{e\mathbf{E}}{m} \cdot \nabla_k [f(\mathbf{x}, \mathbf{k}, t) dV_x dV_k] \\ = \left\{ \frac{\partial}{\partial t} [f(\mathbf{x}, \mathbf{k}, t) dV_x dV_k] \right\}_{\text{coll}} \end{aligned} \quad (18.57)$$

where $\hbar\mathbf{k}$ is used to express the momentum of the electron, m is the effective mass of an electron, and the force on an electron in the presence of an electric field \mathbf{E} is given by $\mathbf{F} = -e\mathbf{E}$. Again assuming that there is a temperature gradient in the x direction and that the distribution is only slightly perturbed from an equilibrium distribution, the Boltzmann transport equation reduces to

$$f' = -\left(\mathbf{v}_x \tau \frac{\partial f_o}{\partial T} \right) \frac{dT}{dx} - \left(\frac{e\tau}{m} \frac{\partial f_o}{\partial v_x} \right) \mathbf{E} \quad (18.58)$$

The following equations can be used to calculate the current density j and heat flux q of a metal based on the number of electrons traveling in a certain direction:

$$j = \int e \cdot v f(\epsilon) D(\epsilon) d\epsilon \quad (18.59)$$

$$q = \int \epsilon \cdot v f(\epsilon) D(\epsilon) d\epsilon \quad (18.60)$$

Again, only the deviation from the equilibrium distribution contributes to the transport properties. Therefore, the current density and heat flux can be written in terms of the thermal gradient and electrical field with four linear coefficients (Ziman, 1960):

$$j = L_{EE}\mathbf{E} + L_{ET} \nabla T \quad (18.61)$$

$$q = L_{TE}\mathbf{E} + L_{TT} \nabla T \quad (18.62)$$

If the thermal gradient is zero, eq. (18.61) reduces to Ohm's law, where $j = \sigma\mathbf{E}$ and $L_{EE} = \sigma$. Using eqs. (18.58) and (18.59), it is possible to solve for the electrical conductivity using the fact that $\partial f / \partial \varepsilon \approx \delta(\varepsilon - \varepsilon_F)$ and $\varepsilon = \frac{1}{2}mv^2$:

$$\sigma = \frac{ne^2\tau}{m} \quad (18.63)$$

If the material is electrically insulated such that $j = 0$ and a thermal gradient is placed across the material, an electric field will be created within the material such that

$$\mathbf{E} = Q \nabla T \rightarrow Q = -\frac{L_{ET}}{L_{EE}} \quad (18.64)$$

where Q is the thermopower of the material. Returning briefly to the case where the thermal gradient is zero, $\nabla T = 0$, there is still a heat flux occurring across the material, as seen from

$$q = L_{TE}E = \Pi j \rightarrow \Pi = \frac{L_{TE}}{L_{EE}} \quad (18.65)$$

where Π is the *Peltier coefficient*. This ability to create a heat flux simply by passing a current through a material is the basis for thermoelectric coolers. The effect of microscale heat transfer in these devices is a topic of current interest and is discussed in Section 18.5.

Whenever a thermal gradient is applied to a material with free electrons, an electric field is established within the material. This electric field actually creates a heat flux that opposes the thermal gradient. Taking this effect into account yields the following expression for the thermal conductivity:

$$K = -\left(L_{TT} - \frac{L_{TE}L_{ET}}{L_{EE}}\right) \quad (18.66)$$

For most metals the electrical conductivity, L_{EE} , is large enough that the thermoelectric effect on the thermal conductivity can be neglected. The less electrically conducting the material, however, the more important it becomes to account for this reduction in the thermal conductivity. If the thermoelectric effects are neglected, the thermal conductivity takes the same form as was found for the case of phonons:

$$K = \frac{1}{3}C_e v \Lambda = \frac{1}{3}C_e v_F^2 \tau \quad (18.67)$$

Using the relaxation time approximation and Boltzmann transport equation expressions for the electrical and thermal conductivity have been derived in terms of a relaxation time, eqs. (18.63) and (18.67). Because both quantities are related linearly to the relaxation time, their ratio is independent of the relaxation time:

$$\frac{K}{\sigma} = \frac{\frac{1}{3}(\pi^2 k_B^2 n / 2eF) v_F^2 \tau}{ne^2 \tau / m} = \frac{\pi^2}{3} \left(\frac{k_B}{e} \right)^2 T \quad (18.68)$$

where eq. (18.21) is used for the electron heat capacity. This result, known as the *Wiedemann-Franz law*, relates the electrical conductivity to the thermal conductivity for metals at all but very low temperature. The proportionality constant is known as the *Lorentz number*:

$$L = \frac{K}{\sigma T} = \frac{\pi^2}{3} \left(\frac{k_B}{e} \right)^2 = 2.45 \times 10^{-8} \text{ W} \cdot \Omega / \text{K}^2 \quad (18.69)$$

18.3.3 Molecular Approach

Recent advances in computational capabilities have increased interest in molecular approaches to solving microscale heat transfer problems. These approaches include lattice dynamic approaches (Tamura et al., 1999), molecular dynamic approaches (Voltz and Chen, 1999; Lukes et al., 2000), and Monte Carlo simulations (Klistner et al., 1988; Woolard et al., 1993). In lattice dynamical calculations the ions are assumed to be at their equilibrium positions, and the intermolecular forces are modeled using appropriate expressions for the types of bonds present. This technique can be very effective in calculating phonon dispersion relations (Tamura et al., 1999) and has also been applied to calculating interfacial properties (Young and Maris, 1989). It is difficult, however, to take into account defects and grain boundaries.

The molecular dynamics approach is very similar; however, more emphasis placed on modeling the interatomic potential and the assumption of a rigid crystalline structure is no longer imposed (Chou et al., 1999). Most molecular dynamics approaches have utilized the Lennard-Jones potential:

$$\phi(r) = 4\xi \left[\left(\frac{r_c}{r} \right)^{12} - \left(\frac{r_c}{r} \right)^6 \right] \quad (18.70)$$

where ξ is a measure of the strength of the attractive forces and r_c is a measure of the radius of the repulsive core. Basically, the ions attract each other with a potential that varies with $1/r^6$ at large separation; however, they become strongly repulsive at short distance due to the Pauli exclusion principle. The noble gases in solid form have been shown to be well characterized by the Lennard-Jones potential; however, some modification is typically required for use of this potential with other crystalline materials. Chou et al. (1999) provide a comprehensive review of the molecular dynamics approaches that have been made on microscale thermophysical problems.

Monte Carlo simulation is very similar to the Boltzmann transfer equation approach, in that the energy carriers are dealt with as particles. In Monte Carlo simulation, the particle's trajectory begins from a particular point traveling in a random

direction and the path is calculated based on parameters that govern the collisional behavior of the particles. The accuracy of this approach is limited by knowledge of the particular collisional events. This technique has been applied to both electron (Woolard et al., 1993) and phonon systems (Klistner et al., 1988).

18.4 OBSERVATION

Numerous experimental methods have been employed to monitor microscale heat transfer phenomena. In an attempt to discuss most of these techniques in a broader context, the methods are grouped into two categories. The techniques are either steady state or transient. The steady-state techniques usually involve thermography or surface temperature measurements. The transient techniques use either a modulated or pulsed heating source and monitor the temperature response as a function of time in order to measure the thermophysical properties. The next distinguishing feature is the manner in which the thermal response is observed. The three most common methods of observing microscale thermal phenomena include thin-film thermocouples, thin-film microbridges, and optical techniques.

Nanometer-scale thermocouples are typically used in conjunction with an atomic force microscope (AFM) (Majumdar, 1999; Shi et al., 2000). This technique is nondestructive because the AFM brings the probe into contact with the sample very carefully. Another series of investigators have used thin-film microbridges, which are usually thinner than 100 nm with a width that depends on the application (Cahill et al., 1994; Lee and Cahill, 1997; Borca-Tasciuc et al., 2000). This technique relies on the fact that the electrical resistance of the microbridge is a strong function of temperature. Because the microbridge must be deposited onto the material of interest, this technique is neither noncontact nor nondestructive. Finally, optical techniques have been employed where a laser is used as either the heating source and/or the thermal probe. The thermal effects can be monitored optically in a number of different ways. One set of techniques relies on the temperature dependence of reflectance and these techniques are referred to as thermoreflectance techniques (Paddock and Eesley, 1986; Hostetler et al., 1997). The thermal expansion that results at the surface can also be used to deflect the probe beam, and the deflection can be related to temperature. These techniques are referred to as *photothermal techniques* (Welsh and Ristau, 1995). Finally, “mirage” techniques use the fact that the air just above the surface is also heated, which causes changes in the index of refraction that bend the probe beam by varying amounts, depending on the change in temperature (Gonzales et al., 2000).

Three different techniques are described in the next few sections. The first technique is scanning thermal microscopy (STM) (Majumdar, 1999). This is an example of the steady-state approach using a nanometer-scale thermocouple. The thermocouple is fabricated onto the tip of an AFM probe. The next technique presented is the 3ω technique, which uses a thin-film microbridge as both the heating source and as a thermal probe (Cahill et al., 1994). This is an example of a modulated transient technique. The last example is the transient thermoreflectance (TTR) technique (Paddock and Eesley, 1986), an optical technique in which a pulsed laser is used to heat and probe the sample. This is an excellent example of a pulsed transient technique.

These examples demonstrate steady-state, modulated, and pulsed transient techniques and the use of thin-film thermocouples, microbridges, and optical methods, respectively, although numerous other combinations or variations of these techniques have been used. Steady-state microbridge techniques have been used to measure thermal boundary resistance (Swartz and Pohl, 1987). For example, an AFM has been used to monitor the expansion and contraction of thin-film materials, which results from a modulated heating source (Varesi and Majumdar, 1998). Lasers have been used as modulated heating sources (Yao, 1987), and to monitor the effects of the pulse heating source on the surface temperature (Kading et al., 1994). A technique called *near-field optical thermometry* was recently developed based on near-field scanning microscopy technology, which uses an optical heating source and seems superior to the diffraction limit associated with far-field optical thermometry (Goodson and Asheghi, 1997).

18.4.1 Scanning Thermal Microscopy

In this section a brief introduction to scanning thermal microscopy (SThM) is presented. Majumdar (1999) published a comprehensive review article that provides more detail and historical development of SThM. Majumdar categorized the majority of techniques into (1) thermovoltage techniques (Shi et al., 2000), (2) electrical resistive techniques (Fiege et al., 1999), and (3) thermal expansion techniques (Varesi and Majumdar, 1998). A single reference has been provided here for each technique, but by no means do these represent the complete literature on the subject.

The majority of SThM experiments fall into the first category of thermovoltage techniques. These techniques require a nanometer-scale thermocouple, which is made

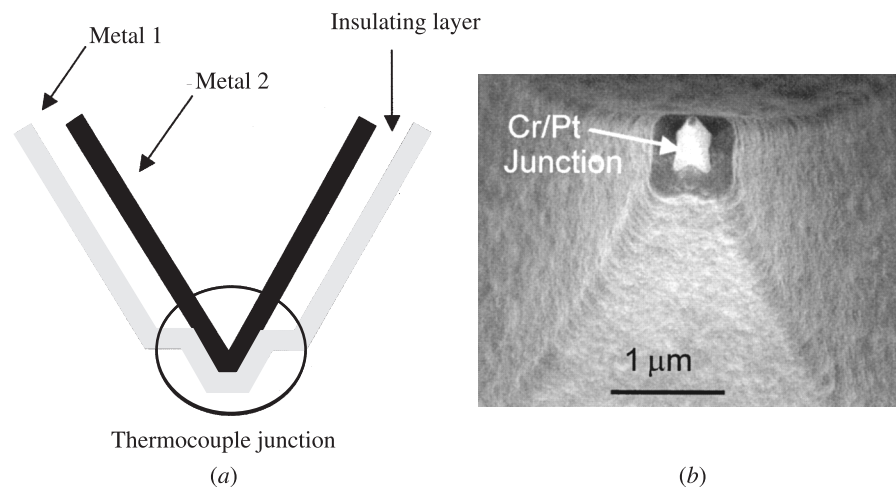


Figure 18.15 (a) Nanometer-scale thermocouple manufactured on the tip of a commercially available AFM cantilever; (b) micrograph of a Cr/Pt thermocouple deposited on a SiN_x cantilever. (Reproduced with permission of L. Shi and A. Majumdar, from Shi et al., 2000.)

by depositing thin metallic films onto commercially available AFM probes. Figure 18.15a is a schematic of the final thermocouple junction. Majumdar (1999) describes several methods for manufacturing these nanometer thermocouples. Figure 18.15b is a micrograph of a Cr/Pt thermocouple junction (Shi et al., 2000). The size of the tip of the thermocouple obviously affects the spatial resolution of the technique. Thermocouples have been fabricated with tip radii between 20 and 50 nm. However, several other factors also affect the spatial resolution. These include the mean free path of the energy carrier of the material to be characterized and the mechanism of heat transfer between the sample and the thermocouple.

Operation of the AFM cantilever is identical to that for a standard AFM probe (Fig. 18.16). The sample is mounted on a x-y-z stage that raises the sample vertically until the sample comes into contact with the cantilever, at which point the cantilever is deflected. The deflection of the cantilever is detected by a reflection of a laser beam off the cantilever. A slight deflection in the cantilever results in a measurable deflection of the laser beam. This information is used in a feedback control loop to maintain contact between the probe and the sample while the sample is being scanned.

Ideally, the thermocouple tip would come into contact with the sample and the thermocouple would quickly reach thermal equilibrium with the sample without affecting the temperature of the surface. Unfortunately, the situation is far from ideal. Thermal energy is transferred to the thermocouple through several mechanisms. There is solid–solid thermal conduction from the sample to the thermocouple where the two are brought into contact. There is also thermal conduction through the gas surrounding the thermocouple tip, and conduction through a liquid layer that condenses in

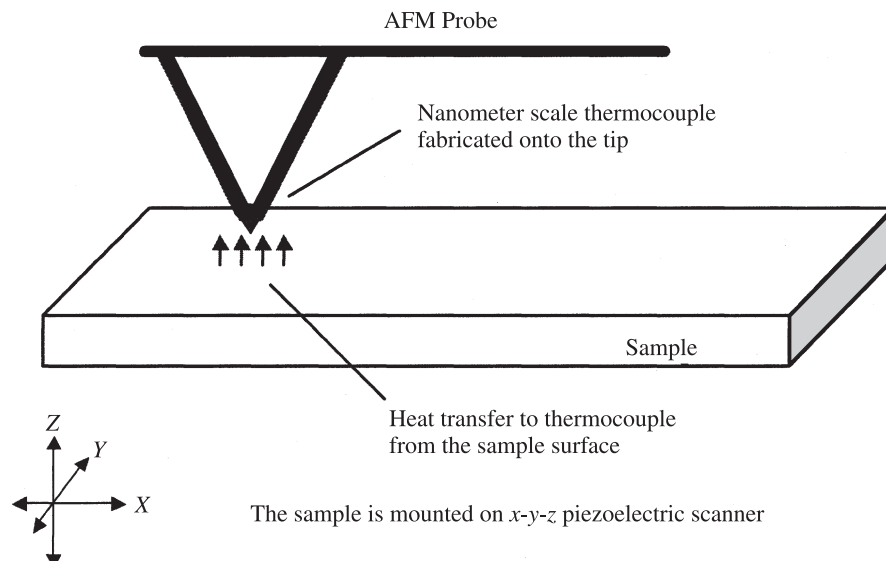


Figure 18.16 Use of a scanning thermal microscope probe to measure the thermal profile of a field-effect transistor.

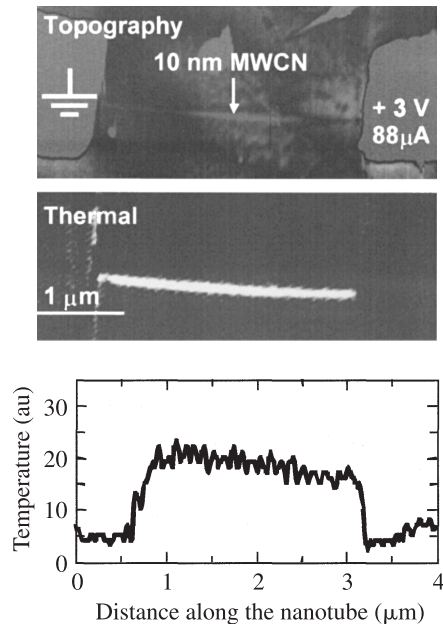


Figure 18.17 Topographical and thermal profile of a multiwalled carbon nanotube that has been heated with a dc electrical current. (Courtesy of L. Shi and A. Majumdar at the University of California–Berkeley.)

the small gap between the tip and the sample. Shi et al. (2000) demonstrated that conduction through this liquid layer dominates the heat transfer under normal atmospheric conditions. Figure 18.17 shows a topographical and thermal image of a 10-nm multiwalled carbon nanotube.

18.4.2 3ω Technique

The 3ω technique has been one of the most widely used and perhaps the most effective technique for measuring the thermophysical properties of dielectric thin films (Cahill, 1990; Lee and Cahill, 1997). Figure 18.18a shows a top view of a microbridge used for the 3ω technique. Figure 18.18b shows a side view of a microbridge that has been deposited onto the thin film to be measured. There are four electrical pads shown in Figure 18.18a; the outer two pads are used to send current through the microbridge, which provides the modulated heating, while the inner two pads are used for measuring the voltage drop across the microbridge.

The current sent through the microbridge is modulated at a certain frequency where $I = I_0 \cos \omega t$. The technique is called the 3ω technique because the temperature oscillations of the sample surface from the modulated current are evident in the microbridge voltage signal at the third harmonic of the current modulation frequency. The microbridge has a resistance R , and the power loss or Joule heating that occurs within the system is proportional to the square of the current:

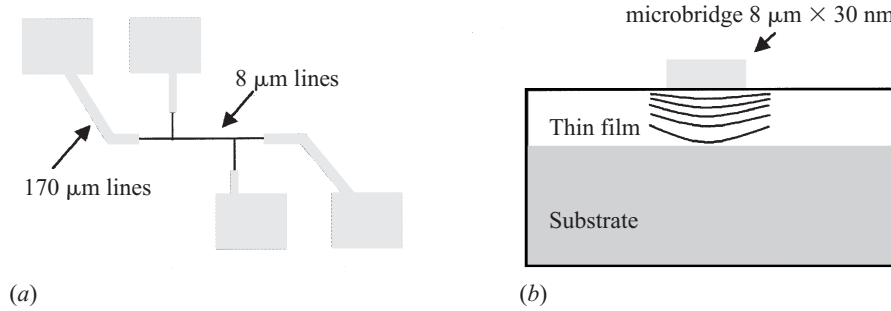


Figure 18.18 (a) Top view of the thin-film microbridge setup used by Lee and Cahill (1997) to measure heat transport in thin dielectric films (from Lee and Cahill, 1997); (b) microbridge deposited onto a dielectric thin-film material. The film thickness and width are much less than the length of the microbridge, making the problem essentially two-dimensional.

$$P = I^2 R = \frac{I_0^2 R}{2} (1 + \cos 2\omega) \quad (18.71)$$

The power loss term has a steady-state component and a sinusoidal term. The modulated component of the heat generation occurs at a frequency of 2ω , which will result in a temperature fluctuation within the system at a frequency of 2ω :

$$T(x, t) = T_s(x) + T_m(x) \cos \omega t \quad (18.72)$$

where T_s is the steady-state temperature distribution and T_m is the amplitude of the temperature oscillations at a frequency of 2ω . Electrical resistance in metals arises due to several electron scattering mechanisms, which include defect scattering, grain boundary scattering, and electron–phonon scattering. As discussed in Section 18.2, the electron–phonon collisional frequency is proportional to the lattice temperature. Therefore, the electrical resistance of metals increases linearly with temperature, $R = R_0 + R_1 T$. This change in the electrical resistance of the film is the basic thermal mechanism that allows for detection of the temperature changes using microbridge techniques:

$$V_{mb} = IR_{mb} = I_0 \cos \omega t [R_0 + R_1 (T_s + T_m \cos 2\omega t)] \quad (18.73)$$

Oscillations occur within the microbridge voltage signal at frequencies of ω and 3ω , where the 3ω signal contains information about the amplitude of the temperature fluctuations of the microbridge. The amplitude of the temperature oscillation is then compared to a thermal model as a function of the heating frequency to determine the effective thermal diffusivity of the underlying material.

One interesting aspect of modulated techniques is that the modulation frequency can be varied, which affects the amount of material that influences the measurement. Essentially, higher oscillation frequencies will only probe the thermal properties near

the surface, while lower frequencies allow more time for diffusion and can be used to probe thicker films. This effect can easily be understood by examining the one-dimensional solution to the heat equation for a semi-infinite material where according to Majumdar (1999), the surface temperature is being modulated at frequency ω_s :

$$T(x, t) \propto \exp\left(-x\sqrt{\frac{\omega_s}{2\alpha_{\text{eff}}}}\right) \exp\left[i\left(\omega_s t - x\sqrt{\frac{\omega_s}{2\alpha_{\text{eff}}}}\right)\right] \quad (18.74)$$

where α_{eff} is the effective thermal diffusivity of the material. These temperature oscillations occurring throughout the film at the modulation frequency are sometimes referred to as *thermal waves* (Rosencwaig et al., 1985). Notice that the amplitude of the temperature oscillation decays exponentially. The penetration depth is inversely proportional to the square root of the modulation frequency:

$$\delta_{rw} = \sqrt{\frac{2\alpha}{\omega}} \quad (18.75)$$

where δ_{rw} is the penetration depth of the thermal wave. Equation (18.74) also demonstrates that the modulation undergoes a phase shift as the thermal wave propagates through the material. This phase shift is a result of the time required for thermal diffusion, which is a relatively slow process. Experimental techniques have been employed that monitor this phase shift and use this information to calculate the thermal diffusivity (Yu et al., 1996).

18.4.3 Transient Thermoreflectance Technique

Ultrashort pulsed lasers with pulse durations of a few picoseconds to subpicoseconds are rapidly becoming viable as an industrial tool. These lasers, used in combination with the transient thermoreflectance (TTR) technique, are capable of measuring the thermal diffusivity of thin films normal to the surface (Paddock and Eesley, 1986; Hostetler et al., 1997). This is an example of a pulsed transient technique where the ultrashort pulsed laser provides the transient phenomena. A pump-probe experimental setup is used to monitor the change in reflectance of the sample surface as a function of time. Once the change in reflectance of the sample surface is known as a function of time, reflectance must be related to temperature. The reflectance of most metals is a function of temperature due to the thermal effects on the absorption from interband transitions. In general, the change in reflectance is linearly related to temperature for small changes in temperature.

The experimental setup is called *pump-probe* because each pulse is split into an intense heating or pump pulse and a weaker probe pulse. The heating pulse is used to generate or initiate the transient phenomena to be observed. The optical path length of the probe pulse is controlled such that the probe can arrive at the sample surface just before, during, or after the heating event. The probe then takes a snapshot of the reflectance at a specific time delay relative to the pump, where the temporal resolution of the snapshot is on the order of the probe pulse duration.

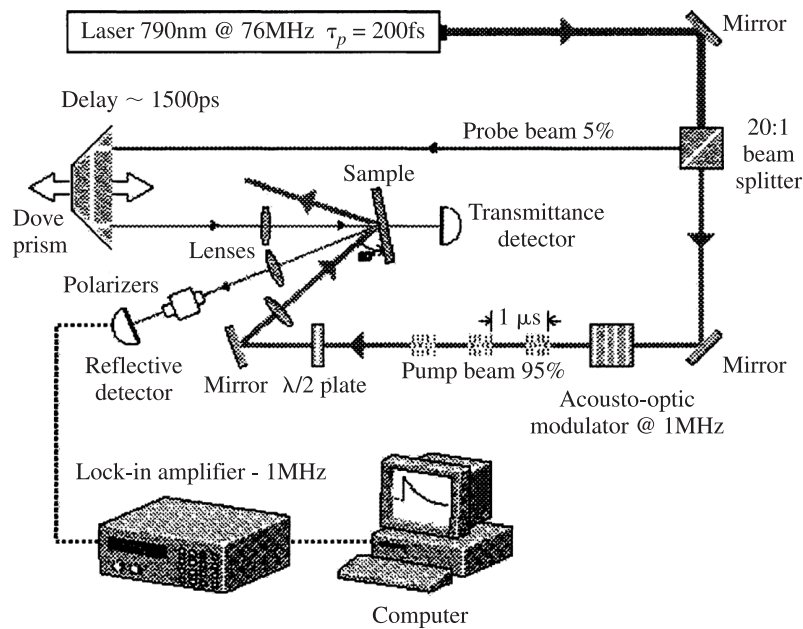


Figure 18.19 Experimental setup for the transient thermoreflectance (TTR) technique.

A schematic of the transient thermoreflectance (TTR) technique is shown in Fig. 18.19. The pump beam is modulated at a frequency on the order of 1 MHz with an acousto-optic modulator. A half-wave plate is then used to rotate the heating beam's polarization parallel to the plane of incidence. The pump beam is focused on the sample surface, which results in an estimated fluence of between 1 and 10 J/m², depending on the spot size and laser power. The probe beam is focused on the center of the region heated by the pump pulse. The probe beam is then sent through a polarizer to filter the scattered pump light and then onto a photodiode.

Because the pump beam is modulated at 1 MHz while the probe beam is not modulated, there is a period of time where the probe is affected by the pump beam, followed by a period where it is not affected. The reflectance of the probe beam, which is always present, will then have a slight modulation occurring at a frequency of 1 MHz. The amplitude of this modulation is proportional to the change in reflectance of the sample surface due to the pump pulse. This amplitude modulation of the probe beam is detected using a lock-in amplifier, which monitors the photodiode response at a frequency of 1 MHz. By slowly changing the optical path length of the probe using a variable delay stage, the change in reflectance of the sample due to the pump pulse (i.e., the thermal relaxation) can be reconstructed on a picosecond time scale.

The advantage of using an ultrashort pulsed laser for this experiment is that the heating caused by the laser pulse is highly localized near the surface. This is not true with longer pulses because thermal energy will diffuse across a 100-nm metal film within several hundred picoseconds. However, ultrashort pulsed lasers deposit their

energy so rapidly that the electrons and phonons within the metal are not always in thermal equilibrium. This phenomena is referred to as *nonequilibrium heating*.

It has been theorized that for subpicosecond laser pulses, the radiant energy is first absorbed by the electrons and then transferred to the lattice (Anisimov et al., 1974). This exchange of energy occurs within a few picoseconds. In 1974, Anisimov presented a two-temperature model, later called the *parabolic two-step (PTS) model*, which assumes that the lattice (or phonons) and electrons can be described by separate temperatures T_l and T_e :

$$C_e(T_e) \frac{\partial T_e}{\partial t} = \frac{\partial}{\partial x} \left[K_e(T_e, T_l) \frac{\partial T_e}{\partial x} \right] - G(T_e - T_l) + S(x, t) \quad (18.76a)$$

$$C_l \frac{\partial T_l}{\partial t} = G(T_e - T_l) \quad (18.76b)$$

The electron–phonon coupling factor G is a material property that represents the rate of energy transfer between the electrons and the lattice. The heat capacity of the electrons and the lattice, C_e and C_l , and the thermal conductivity of the electrons K_e are also material properties. The appropriate expressions for the electron heat capacity was given as eq. (18.21). The electron thermal conductivity can be determined to be $K_e = K_{eq}(T_e/T_l)$ using eqs. (18.32)–(18.35).

Thermal diffusivity of the thin film can be obtained by comparing the transient reflectance response to the thermal model presented as eqs. (18.76a) and (18.76b). This model requires that the electron–phonon coupling factor be known, however.

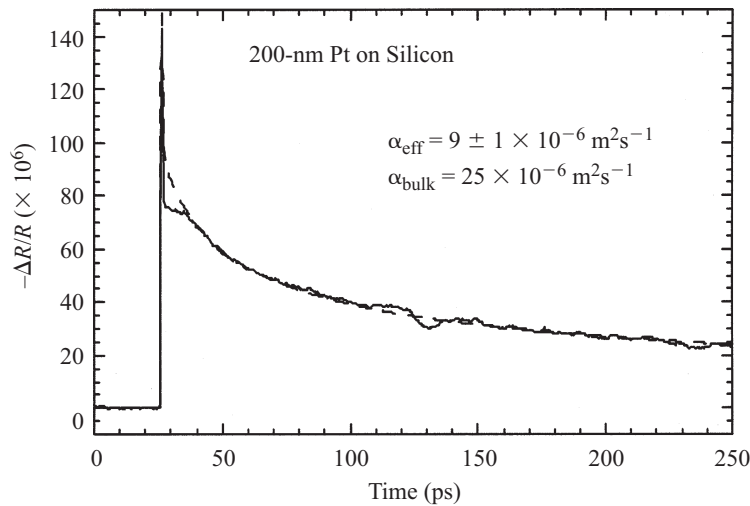


Figure 18.20 Change in reflectance of a 200-nm Pt thin film on silicon where the phase and magnitude of the signal have been taken into account. The experimental results are compared to the PTS model to determine the thermal diffusivity.

While values are available in the literature for most metals, the electron–phonon coupling factor can be affected by the microstructure of the film (Elsayed-Ali et al., 1991). The electron–phonon coupling factor can be measured with the TTR technique using an optically thin film to minimize the effects of diffusion. The electron–phonon coupling can then be directly observed in the first few picoseconds of the transient response (Hostetler et al., 1999). Figure 18.20 shows a TTR scan taken on a 200-nm Pt film evaporated onto a silicon substrate. The value of the thermal diffusivity was determined to be $9 \pm 1 \times 10^6 \text{ m}^2/\text{s}$ using a least squares fitting routine. This value is significantly less than the bulk value for platinum.

18.5 APPLICATIONS

Microscale heat transfer was defined in Section 18.1 as the study of heat transfer when the individual carriers must be considered or when the continuum model breaks down. Several examples are presented next that illustrate how microscale heat transfer is of critical importance to the microelectronics industry. Then thermal transport in multilayer and superlattice structures is covered. The increased scattering of energy carriers leads to increased thermal resistance within these materials.

18.5.1 Microelectronics Applications

To keep pace with the demand for faster, smaller devices, there is a continual need for materials with lower dielectric constants. Unfortunately, materials that are good electrical insulators are also typically good thermal insulators. Increased operating temperatures in these new devices would lead to increases in electrical crosstalk and electromigration, which would defeat the purpose of employing a better electrical insulator. These thermal considerations can directly affect the ultimate packing density of new devices (Goodson and Flik, 1992). Currently, continuum models are sufficient to model the thermal performance of these devices, and microscale thermal effects are usually taken into account by employing measured material properties for the thin-film materials. These properties are measured using the methods described in Section 18.4. The effective use of these material properties is typically the subject of electronic cooling, which represents another large area of research. Novel phase-change materials (Pal and Joshi, 1997), and micro heat pipes (Peterson et al., 1998) are just a few examples of cutting-edge research activities aimed at improvements in device thermal management.

Traditional metal-oxide semiconductor field-effect transistors (MOSFETs) are manufactured directly on the bulk silicon substrate. Because crystalline silicon is a very good thermal conductor, the removal of thermal energy is usually not a primary concern. However, because these transistors are made directly on the silicon substrate, there can be, at most, one layer of transistors. Silicon-on-insulator (SOI) transistors, which are not limited to a single layer, are extremely desirable for use in manufacturing a three-dimensional chip. The presence of an insulating layer between the device and the silicon substrate also reduces the leakage current, the threshold

voltage, and the junction capacitance of the device. While these reductions all represent improvements, the insulating layer also decreases the ability of the device to dissipate heat. SOI transistors are an excellent example of a modern microelectronics device in which microscale heat transfer plays an important role in the overall device performance. Ju and Goodson (1999) cover the subject of microscale heat conduction in integrated circuits in great detail.

Figure 18.21 is a basic schematic of a SOI transistor where the individual components have been labeled. This device is a field-effect transistor, which means that when a voltage is applied to the gate, a small conductive channel is created in the doped silicon device layer just underneath the gate. This conductive channel allows current to flow from the source to the drain. However, the majority of the resistive heating of the device occurs within this channel. This results in highly localized heating in the silicon layer underneath the gate. The presence of the insulating oxide layer forces the thermal energy to propagate through the silicon device layer and then through the metal leads of the source and drain. The thickness of the silicon device layer can be less than 100 nm, which is on the order of the mean free path of a phonon in silicon. Several experimental studies have been performed to quantify size effects in thin silicon films. The source and drain lines are made of metallic materials which act like fins, moving the thermal energy away from the device (Goodson and Flik, 1992). The thickness of these metal leads is currently on the order of several hundred nanometers, which is greater than the mean free path of an electron. However, as these dimensions continue to diminish, continuum models will no longer be applicable.

Another interesting thermal effect that occurs in field-effect transistors which falls into the area of microscale heat transfer is nonequilibrium Joule heating. Nonequilibrium Joule heating can occur in the area of the drain due to the very high electric field that is established in the region just underneath the gate. The strength of this electric field is inversely proportional to the channel length. The channel length directly

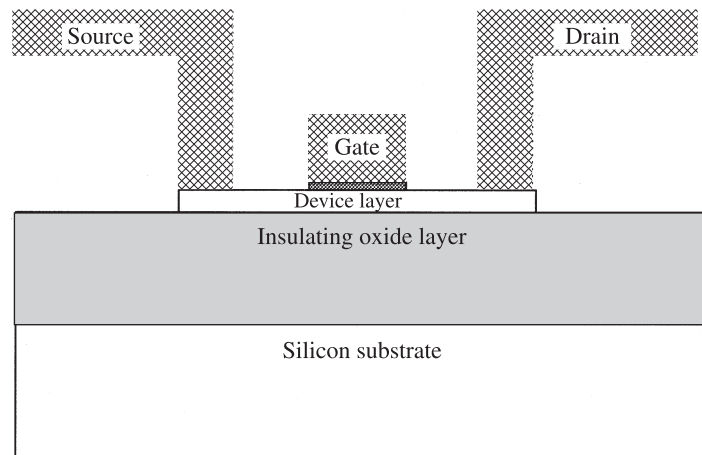


Figure 18.21 Individual components of a silicon-on-insulator (SOI) field-effect transistor.

affects the time required for the transistor to switch; therefore, efforts are constantly under way to reduce the channel length. Operation of a field-effect transistor with a channel length of 61 nm was recently demonstrated (Timp, 1997), and manufacturing of channel lengths with sub-100-nm dimensions is expected within the first decade of the twenty-first century. The high electric field present between the source and the drain creates highly energetic electrons, which are not in thermal equilibrium with the lattice when they arrive at the drain. Lai and Majumdar (1996) present a simple thermal and electrical model for submicron silicon semiconductor devices using hydrodynamic equations for the electron system and conservation equations for the optical and acoustic phonons. Another thermal analysis of nonequilibrium Joule heating was performed on GaAs metal semiconductor field-effect transistors (Fushinobu et al., 1995). In both cases, the nonequilibrium electron temperatures were predicted to be on the order of 1000 K, while changes in the lattice temperature were on the order of tens of kelvin. This behavior is very similar to the nonequilibrium heating that occurs in metals and semiconductors when heated with ultrashort pulsed lasers, as discussed in Section 18.4.

18.5.2 Multilayer Thin-Film Structures

Multilayer thin films and superlattice structures are currently being utilized in numerous modern devices due to their unique material properties. One example is giant magnetoresistance (GMR) technology, which holds great promise for increasing memory density, access speed, and power requirements for memory maintenance. GMR devices are created using multilayer metallic superlattices where the individual layers are on the order of a few nanometers (Baibich et al., 1988). Quantum well lasers are another example of multilayer thin-film structures, where the layer thickness is on the order of the mean free path of the heat carrier. A certain amount of thermal resistance is associated with each interface within the multilayer structure, due to phonon scattering that occurs at each interface. Yu et al. (1995) showed that the thermal conductivity of a 700 Å/700 Å GaAs/AlAs superlattice is significantly less than that of the corresponding bulk materials but larger than that of the corresponding alloy. Reduced values for the thermophysical properties of superlattice materials have been incorporated into continuum models to predict the increases in operating temperatures. One example is a thermal analysis performed on vertical cavity surface-emitting laser diodes (VCSELs), which showed a significant increase in the operating temperature (Norris et al., 1994).

Recently, the increased thermal resistance associated with superlattice structures has been under investigation as a means of improving the performance of thermoelectric materials (Hicks and Dresselhaus, 1993). Reduced thermal transport properties typically represent a nuisance effect, causing devices to operate at higher, less desirable temperatures. In the case of thermoelectric materials, however, the reduction in thermal transport is being used to engineer better materials. Heat transfer through the thermoelectric device significantly reduces the overall efficiency, and new materials are being fabricated using multilayer superlattice structures to reduce thermal transport by phonons. Figure 18.22 shows a schematic of a basic thermoelectric cooler.

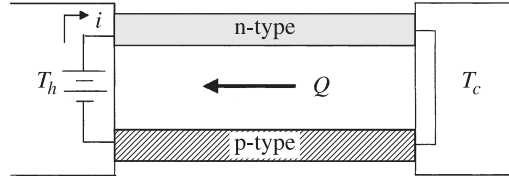


Figure 18.22 Thermoelectric device fabricated using n - and p -type doped semiconductor materials.

Because electrons carry both thermal energy and charge, the thermal and electrical properties of metals are interrelated. As was shown in Section 18.3, the current density and heat flux can be written in terms of the thermal gradient and electrical field with four linear coefficients (Ziman, 1960):

$$j = L_{EE} E + L_{ET} \nabla T \quad (18.61)$$

$$q = L_{TE} E + L_{TT} \nabla T \quad (18.62)$$

From these equations we can see that in the case of zero current, an electric field will be present whenever a thermal gradient exists. This phenomenon is referred to as the *Seebeck effect*. The thermoelectric power, or *Seebeck coefficient*, can be expressed as

$$S = \frac{L_{ET}}{L_{EE}} \quad (18.77)$$

The higher the thermoelectric power, the more energy the device can move from the cold side of the device to the hot side. However, the higher the thermopower, the more electrically resistive the device becomes, which creates more thermal energy due to Joule heating, some of which is conducted to the cold side of the device. In addition, thermal conduction through the device from the hot side to the cold side reduces the efficiency. The thermoelectric figure of merit, Z , accounts for these conflicting effects and is given by

$$Z = \frac{S^2 \sigma}{K} \quad (18.78)$$

where σ is the electrical conductivity and K is the thermal conductivity. As mentioned previously, increasing the thermoelectric power leads to a decrease in the electrical conductivity. The thermal conductivity has two components, one from phonons and another from electrons in the semiconductor:

$$K = K_e + K_p \quad (18.79)$$

The electronic thermal conductivity is related to the electrical conductivity through the Wiedemann–Franz law discussed in Section 18.3. However, any reduction in

thermal conduction from phonons through the device can increase the figure of merit. Some examples of materials that have high values of Z include Bi_2Te_3 and SiGe alloys.

It has been shown that depending on the layer thickness, it is possible for superlattice materials to have a thermal conductivity that is less than that of the corresponding alloy (Borca-Tasçiuc et al., 2000). While alloying materials typically reduce the thermal properties due to increased scattering sites, the interface between two materials can also be a strong source of thermal resistance. This resistance, called *thermal boundary resistance*, is caused by either the reflection of heat carriers at the interface or by differences in the phonon density of states between the materials (Swartz and Pohl, 1989). Figure 18.23 shows the cross-plane thermal conductivity of several SiGe superlattice materials with different periods. The thermal conductivity was measured using a differential 3ω method (Borca-Tasçiuc et al., 2000). The thermal conductivity was approximately 50% less than the alloy for the samples with 9- and 14.4-nm periods. The sample with the smallest period, 4 nm, had a thermal conductivity closer to that of the alloy.

It has recently been proposed that two-dimensional structures may be able to achieve higher thermoelectric figures of merit. Hicks et al. (1996) propose that these two-dimensional structures can be prepared in the form of quantum well structures. In our earlier discussion, the multilayer thermoelectric devices were oriented in the cross-plane direction to reduce thermal conduction. The devices proposed would be oriented in the in-plane direction to capitalize on increased thermoelectric effects.

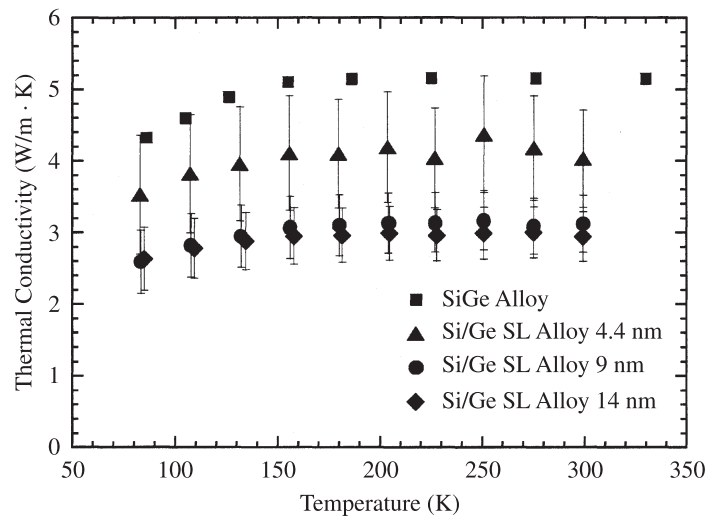


Figure 18.23 Temperature dependence of the thermal conductivity of Si/Ge superlattices of varying period as compared to a SiGe alloy material. (Reproduced with permission of Theodorian Borca-Tasçiuc.)

18.6 CONCLUSIONS

Microscale heat transfer is a new subject in concept but not in practice. The microscopic study of the thermal properties of solids has been a topic within condensed matter physics for at least five decades. As discussed in Section 18.1, many of the thermal properties of bulk materials can be adequately explained with rather simple models of the electron and lattice systems. These concepts provide the foundation necessary to tackle many of the problems facing microscale heat transfer.

This chapter has provided an overview of the primary theoretical methods used for approaching microscale heat transfer problems. The first and simplest approach is simply a continuum model, where microscale effects are taken into account by employing accurate values for the thermophysical properties of the thin-film materials employed in the device. When the length scales of the thermal problem are on the order of the mean free path of the energy carrier, however, continuum models are no longer applicable. The Boltzmann transport equation was discussed and can be used to solve a number of problems; however, to model the collisional term, certain assumptions must be made. Finally, molecular dynamics and Monte Carlo simulations were discussed briefly, but again, these techniques typically require a large number of assumptions, which limit the accuracy.

Several methods for observing the effects of microscale heat transfer were discussed. To see the effects of microscale heat transfer, the observer must look on very short time or length scales, and this often requires the development of new experimental techniques. Scanning thermal microscopy (SThM) was given as an example of a technique capable of resolving surface temperature on nanometer length scales, and the transient thermoreflectance technique was given as an example of a technique used to monitor transport phenomena on a picosecond timescale. Development of a technique capable of both ultrashort length scale and ultrashort time scale measurements remains a challenge.

Finally, a few applications were presented that demonstrate the importance of considering microscale heat transfer. As the nanotechnology revolution continues, the need for accurate modeling of thermal transport on ultrashort time and length scales will be vital to the success of many new devices. The distinction between thermal engineers and physicists will begin to blur, as engineers continue to draw on the concepts of condensed matter physics to explain and predict the transport properties of microscopic energy carriers. These advances require the education of a new breed of thermal engineers; those trained in modern physics as well as in mechanics. This is an exciting period in the field of heat transfer and many challenges remain.

NOMENCLATURE

Roman Letter Symbols

A	electron-electron scattering coefficient ($\text{K}^{-2}\text{s}^{-1}$)
a	interatomic spacing (m)
\mathbf{a}_i	primitive lattice vectors (m)

B	electron-phonon scattering coefficient ($\text{K}^{-1}\text{s}^{-1}$)
\mathbf{b}_i	reciprocal primitive lattice vectors (m^{-1})
C	heat capacity ($\text{Jm}^{-3}\text{K}^{-1}$)
c	speed of sound (ms^{-1})
D	density of states
E	electric field (Vm^{-1})
e	electrical charge (C)
F	force (N)
f	Fermi-Dirac distribution
f'	change in Fermi-Dirac distribution
G	electron-phonon coupling factor ($\text{Wm}^{-3}\text{K}^{-1}$)
\hbar	Planck's constant (eVs)
I	current (A)
j	current density (Am^{-2})
K	thermal conductivity ($\text{Wm}^{-1}\text{K}^{-1}$)
K	spring constant (NM^{-1})
\mathbf{k}	wavevector (m^{-1})
k_B	Boltzmann constant (eVK^{-1})
L	length (m)
\mathcal{L}	Lorentz number (WOhmK^{-2})
L_{ET}	thermoelectric coefficient ($\text{Am}^{-1}\text{K}^{-1}$)
L_{EE}	thermoelectric coefficient ($\text{Am}^{-1}\text{V}^{-1}$)
L_{TE}	thermoelectric coefficient ($\text{Wm}^{-1}\text{V}^{-1}$)
L_{TT}	thermoelectric coefficient ($\text{Wm}^{-1}\text{K}^{-1}$)
l	mean free path (m)
M	mass of an ion (kg)
m	effective mass of an electron (kg)
N	Bose-Einstein distribution
N_l	number of lattice sites
N_e	number of free electrons
n	integer
n_e	electron number density (m^{-3})
P	momentum (kgms^{-1})
\mathcal{P}	power (W)
Q	thermopower (VK^{-1})
q	heat flux (Wm^{-2})
\mathbf{R}	position of lattice site (m)
\mathcal{R}	resistance (Ohms)
\mathbf{r}	position of ions (m)
r_c	radius of repulsive core (m)
S	heating source (Wm^{-3})
S_b	Seebeck coefficient (VK^{-1})
T	temperature (K)
t	time (s)
U	internal energy (J)

u	specific internal energy (Jkg^{-1})
u	displacement (m)
V	volume (m^3)
\mathcal{V}	potential difference (V)
v	velocity (ms^{-1})
v	displacement (m)
x	direction normal to surface (m)
Z	thermoelectric figure of merit

Greek Symbols

α	thermal diffusivity (m^2s^{-1})
δ_{tw}	thermal wave penetration depth (m)
ε	electron energy (eV)
ϕ	interatomic potential (N)
μ	chemical potential (eV)
Π	Peltier coefficient (WA^{-1})
θ_D	Debye temperature (K)
σ	electrical conductivity ($\text{Am}^{-1}\text{V}^{-1}$)
τ	relaxation time (s)
ω	frequency (rad)
ν	collisional frequency (s^{-1})
ξ	strength of interatomic forces (N)

Subscripts

b	boundary
e	electron
ee	electron-electron
eff	effective
ep	electron-phonon
D	Debye
d	defect
F	Fermi
g	group
k	wavevector
l	lattice
m	modulated
n	n^{th} lattice site
o	equilibrium
P	momentum
pp	phonon-phonon
rms	root mean square
s	phonon branches
ss	steady state
tot	total

REFERENCES

- Anisimov, S. I., Kapeliovich, B. L., and Perelman, T. L. (1974). Electron Emission from Metal Surfaces Exposed to Ultrashort Laser Pulses, *Sov. Phys. JETP*, 39, 375–377.
- Ashcroft, N. W., and Mermin, N. D. (1976). *Solid State Physics*, Saunders College Publishing, Fort Worth, TX.
- Baibich, M. N., Broto, J. M., Fert, A., Dau, F. N. V., and Petroff, F. (1988). Giant Magnetoresistance of (001)Fe/(001)Cr Magnetic Superlattices, *Phys. Rev. Lett.*, 61, 2472–2475.
- Borca-Tasçiuc, T., Liu, W., Zeng, T., Song, D. W., Moore, C. D., Chen, G., Wang, K. L., Goorsky, M. S., Radetic, T., and Gronsky, T. (2000). Thermal Conductivity of Symetrically Strained Si/Ge Superlattices, *Superlattices Microstruct.*, 28, 199–206.
- Brockhouse, B. N., Arase, T., Caglioti, G., Rao, K. R., and Wods, A. D. B. (1962). Crystal Dynamics of Lead, I: Dispersion Curves at 100 K, *Phys. Rev.*, 128, 1099–1111.
- Cahill, D. G. (1990). Thermal Conductivity Measurements from 30–750 K: The 3ω Method, *Rev. Sci. Instrum.*, 61, 802–808.
- Cahill, D. G., and Pohl, R. O. (1988). Lattice Vibrations and Heat Transport in Crystals and Glasses, *Annu. Rev. Phys. Chem.*, 39, 93–121.
- Cahill, D. G., Katiyar, M., and Abelson, J. R. (1994). Thermal Conductivity of a-Si:H Thin Films, *Phys. Rev. B*, 50, 6077–6081.
- Chou, F. C., Lukes, J. R., Liang, X. G., Takahashi, K., and Tien, C. L. (1999). Molecular Dynamics in Microscale Thermophysical Engineering, in *Annual Review of Heat Transfer*, C. L. Tien, ed., Begell House, New York, pp. 141–176.
- Elsayed-Ali, H. E., Juhasz, T., Smith, G. O., and Bron, W. E. (1991). Femtosecond Thermorefectivity and Thermotransmissivity of Polycrystalline and Single-Crystalline Gold Films, *Phys. Rev. B*, 43, 4488–4491.
- Fiege, G. B. M., Altes, A., Heiderhoff, R., and Balk, L. J. (1999). Quantitative Thermal Conductivity Measurements with Nanometre Resolution, *J. Phys. D Appl. Phys.*, 32, L13–L17.
- Fuchs, K. (1938). The Conductivity of Thin Metallic Films According to the Electron Theory of Metals, *Proc. Cambridge Philos. Soc.*, 34, 100–108.
- Fushinobu, K., Majumdar, A., and Hijikata, K. (1995). Heat Generation and Transport in Submicron Semiconductor Devices, *J. Heat Transfer*, 117, 25–31.
- Gonzales, E. J., Bonevich, J. E., Stafford, G. R., White, G., and Josell, D. (2000). Thermal Transport through Thin Films: Mirage Technique Measurements on Aluminum/Titanium Multilayers, *J. Mater. Res.*, 15, 764–771.
- Goodson, K. E., and Asheghi, M. (1997). Near-Field Optical Thermometry, *Microscale Thermophys. Eng.*, 1, 225–235.
- Goodson, K. E., and Flik, M. I. (1992). Effect of Microscale Thermal Conduction on the Packing Limit of Silicon-on-Insulator Electronic Devices, *IEEE Trans. Components Hybrids Manuf. Technol.*, 15, 715–722.
- Hicks, L. D., and Dresselhaus, M. S. (1993). Effect of Quantum-Well Structures on the Thermoelectric Figure of Merit, *Phys. Rev. B*, 47, 12727–12731.
- Hicks, L. D., Harmon, T. C., Sun, X., and Dresselhaus, M. S. (1996). Experimental Study of the Effect of Quantum-Well Structures on the Thermoelectric Figure of Merit, *Phys. Rev. B*, 53, R10493–R10496.

- Hostetler, J. L., Smith, A. N., and Norris, P. M. (1997). Thin Film Thermal Conductivity and Thickness Measurements Using Picosecond Ultrasonics, *Microscale Thermophys. Eng.*, 1, 237–244.
- Hostetler, J. L., Smith, A. N., and Norris, P. M. (1999). Measurement of the Electron–Phonon Coupling Factor Dependence on Film Thickness and Grain Size in Au, Cr and Al, *Appl. Opt.*, 38, 3614–3620.
- Joseph, D. D., and Preziosi, L. (1989). Heat Waves, *Rev. Mod. Phys.*, 61, 41–73.
- Ju, Y. S., and Goodson, K. E. (1999). *Microscale Heat Conduction in Integrated Circuits and Their Constituent Films*, Kluwer Academic, Boston.
- Kading, O. W., Shurk, H., and Goodson, K. E. (1994). Thermal Conduction in Metallized Silicon-Dioxide Layers on Silicon, *Appl. Phys. Lett.*, 65, 1629–1631.
- Kittel, C. (1996). *Introduction to Solid State Physics*, Wiley, New York.
- Kittel, C., and Kroemer, H. (1980). *Thermal Physics*, W.H. Freeman, San Francisco.
- Klistner, T., Vanleve, J. E., Fischer, H. E., and Pohl, R. O. (1988). Phonon Radiative Heat Transfer and Surface Scattering, *Phys. Rev. B*, 38, 7576–7594.
- Lai, J., and Majumdar, A. (1996). Concurrent Thermal and Electrical Modeling of Sub-micrometer Silicon Devices, *J. Appl. Phys.*, 79, 7353–7361.
- Lee, S. M., and Cahill, D. G. (1997). Heat Transport in Thin Dielectric Films, *J. Appl. Phys.*, 81, 2590–2595.
- Lukes, J. R., Li, D. Y., Liang, X. G., and Tien, C. L. (2000). Molecular Dynamics Study of Solid Thin-Film Thermal Conductivity, *J. Heat Transfer*, 122, 536–543.
- Majumdar, A. (1993). Microscale Heat Conduction in Dielectric Thin Films, *J. Heat Transfer*, 115, 7–16.
- Majumdar, A. (1998). Microscale Energy Transport in Solids, in *Microscale Energy Transport*, C. L. Tien, A. Majumdar, and F. M. Gerner, eds., Taylor & Francis, Washington, DC, pp. 3–94.
- Majumdar, A. (1999). Scanning Thermal Microscopy, *Annu. Rev. Mater. Sci.*, 29, 505–585.
- Mayadas, A. F., Shatzkes, M., and Janak, J. F. (1969). Electrical Resistivity Model for Polycrystalline Films: The Case of Specular Reflection at External Surfaces, *Appl. Phys. Lett.*, 14, 345–347.
- Mott, N. F. (1993). *Conduction in Non-crystalline materials*, Oxford University Press, Oxford.
- Norris, P. M., Chen, G., and Tien, C. L. (1994). Size-Effects on the Temperature Rise in Vertical Cavity Surface-Emitting Laser Diodes, *Int. J. Heat Mass Transfer*, 37, 9–14.
- Paddock, C. A., and Eesley, G. L. (1986). Transient Thermoreflectance from Thin Metal Films, *J. Appl. Phys.*, 60, 285–290.
- Pal, D., and Joshi, Y. K. (1997). Application of Phase Change Materials to Thermal Control of Electronic Modules: A Computational Study, *J. Electron. Packag.*, 119, 40–50.
- Peterson, G. P., Swanson, L. W., and Gerner, F. M. (1998). Micro Heat Pipes, in *Microscale Energy Transport*, C. L. Tien, A. Majumdar, and F. M. Gerner, eds., Taylor & Francis, Washington, DC, pp. 295–337.
- Powell, R. W., Ho, C. Y., and Liley, P. E. (1966). *Thermal Conductivity of Selected Elements*, U.S. Government Printing Office, Washington, DC.
- Powell, R. W., Ho, C. Y., and Liley, P. E. (1974). *Thermal Conductivity of the Elements: A Comprehensive Review*, American Chemical Society, Washington, DC.

- Rosencwaig, A., Opsal, J., Smith, W. L., and Willenborg, D. L. (1985). Detection of Thermal Waves through Optical Reflectance, *Appl. Phys. Lett.*, 46, 1013–1015.
- Shi, L., Plyasunov, S., Bachtold, A., McEuen, P. L., and Majumdar, A. (2000). Scanning Thermal Microscopy of Carbon Nanotubes Using Batch-Fabricated Probes, *Appl. Phys. Lett.*, 77, 4295–4297.
- Swartz, E. T., and Pohl, R. O. (1987). Thermal Resistance at Interfaces, *Appl. Phys. Lett.*, 51, 2200–2202.
- Swartz, E. T., and Pohl, R. O. (1989). Thermal Boundary Resistance, *Rev. Mod. Phys.*, 61, 605–668.
- Tamura, S., Tanaka, Y., and Maris, H. J. (1999). Phonon Group-Velocity and Thermal Conduction in Superlattices, *Phys. Rev. B*, 60, 2627–2630.
- Timp, G. (1997). Low Leakage, Ultra-thin Gate Oxides for Extremely High Performance Sub-100 nm nMOSFETs, *IEDM Tech. Dig.*, Cat. No. 97CH36103, 930–932.
- Varesi, J., and Majumdar, A. (1998). Scanning Joule Expansion Microscopy at Nanometer Scales, *Appl. Phys. Lett.*, 72, 37–39.
- Voltz, S., and Chen, G. (1999). Molecular Dynamics Simulation of Thermal Conductivity of Silicon Nanowires, *Appl. Phys. Lett.*, 75, 2056–2058.
- Weast, R. C., Astle, M. J., and Beyer, W. H., eds. (1985). *CRC Handbook of Chemistry and Physics*, CRC Press, Boca Raton, FL.
- Welsh, E., and Ristau, D. (1995). Photothermal Measurements on Optical Thin Films, *Appl. Opt.*, 34, 7239–7253.
- Wilson, A. H. (1954). *The Theory of Metals*, Cambridge University Press, Cambridge.
- Woolard, D. L., Tian, H., Littlejohn, M. A., Kim, K. W., Trew, R. J., Leong, M. K., and Tang, T. W. (1993). Construction of Higher-Moment Terms in the Hydrodynamic Electron-Transport Model, *J. Appl. Phys.*, 74, 6197–6207.
- Yao, T. (1987). Thermal Properties of AlAs/GaAs Superlattices, *Appl. Phys. Lett.*, 51, 1798–1800.
- Young, D. A., and Maris, H. J. (1989). Lattice-Dynamical Calculation of the Kapitza Resistance between FCC Lattices, *Phys. Rev. B*, 40, 3685–3693.
- Yu, X. Y., Chen, G., Verma, A., and Smith, J. S. (1995). Temperature Dependence of Thermo-physical Properties of GaAs/AlAs Periodic Structure, *Appl. Phys. Lett.*, 67, 3554–3556.
- Yu, X. Y., Zhang, L., and Chen, G. (1996). Thermal-Wave Measurements of Thin-Film Thermal Diffusivity with Different Laser Beam Configurations, *Rev. Sci. Instrum.*, 67, 2312–2316.
- Ziman, J. M. (1960). *Electrons and Phonons*, Oxford University Press, London.

